CrossMark

J. Fluid Mech. (2018), *vol.* 848, *pp.* 788–820. © Cambridge University Press 2018
doi:10.1017/jfm.2018.387

Weakly sheared turbulent flows generated by multiscale inhomogeneous grids

Shaokai Zheng[1,†], P. J. K. Bruce[1], J. M. R. Graham[1] and J. C. Vassilicos[1,†]

[1]Department of Aeronautics, Imperial College London, London, SW7 2AZ, UK

(Received 6 July 2017; revised 25 March 2018; accepted 4 May 2018;
first published online 13 June 2018)

A group of three multiscale inhomogeneous grids have been tested to generate different types of turbulent shear flows with different mean shear rate and turbulence intensity profiles. Cross hot-wire measurements were taken in a wind tunnel with Reynolds number Re_D of 6000–20 000, based on the width of the vertical bars of the grid and the incoming flow velocity. The effect of local drag coefficient C_D on the mean velocity profile is discussed first, and then by modifying the vertical bars to obtain a uniform aspect ratio the mean velocity profile is shown to be predictable using the local blockage ratio profile. It is also shown that, at a streamwise location $x = x_m$, the turbulence intensity profile along the vertical direction $u'(y)$ scales with the wake interaction length $x_{*,n}^{peak} = 0.21 g_n^2/(\alpha C_D w_n)$ (α is a constant characterizing the incoming flow condition, and g_n, w_n are the gap and width of the vertical bars, respectively, at layer n) such that $(u'/U_n)^2\beta^2(C_D w_n/x_{*,n}^{peak})^{-1} \sim (x_m/x_{*,n}^{peak})^b$, where β is a constant determined by the free-stream turbulence level, U_n is the local mean velocity and b is a dimensionless power law constant. A general framework of grid design method based on these scalings is proposed and discussed. From the evolution of the shear stress coefficient $\rho(x)$, integral length scale $L(x)$ and the dissipation coefficient $C_\epsilon(x)$, a simple turbulent kinetic energy model is proposed that describes the evolution of our grid generated turbulence field using one centreline measurement and one vertical profile of $u'(y)$ at the beginning of the evolution. The results calculated from our model agree well with our measurements in the streamwise extent up to $x/H \approx 2.5$, where H is the height of the grid, suggesting that it might be possible to design some shear flows with desired mean velocity and turbulence intensity profiles by designing the geometry of a passive grid.

Key words: turbulent flows

1. Introduction

The study of grid turbulence has been of interest for decades. Regular grids made of bars with uniform mesh size have been used by many to study homogeneous/isotropic turbulence (e.g. Comte-Bellot & Corrsin 1966, 1971; Gad-El-Hak & Corrsin 1974; Mohamed & Larue 1990; Mydlarski & Warhaft 1996; Cardesa, Nickels & Dawson 2012). Other efforts have also been made to develop different types of devices to produce shear flows in wind tunnel experiments. Some of the most popular methods

† Email addresses for correspondence: s.zheng13@imperial.ac.uk, j.c.vassilicos@imperial.ac.uk

https://doi.org/10.1017/jfm.2018.387 Published online by Cambridge University Press

are briefly reviewed here, and reviews of the earlier methods can be found in Lawson (1968) and Laws & Livesey (1978). Here and for the rest of the discussion, x, y, z represent the streamwise, vertical and transverse direction, respectively.

1.1. *Shear generating methods*

Several methods have been proposed to generate shear flows in laboratories. One of the methods is to use wire gauzes to modify the local solidity, and consequently produce a mean velocity gradient. The effect of flow passing through wire gauzes was described in detail by Taylor *et al.* (1949). Then by using resistance and deflection coefficients as grid properties, a theoretical method of grid design was offered by Owen & Zienkiewicz (1957) relating the downstream mean velocity profile to the spacing of the wires, and a uniform shear flow was produced in their study using parallel wires of diameter $d = 3.175$ mm. This theory was further generalized by Elder (1959) to non-uniform gauze with arbitrary shapes. Elder (1959) tested his theory on linear and parabolic gauzes, and proposed a gauze shape to generate a linear shear flow. Rose (1966) followed the same method and showed that the shape of the generated downstream mean velocity profile was persistent. The later studies of Livesey & Laws (1973*a*) on flow through curved gauze screens proposed a modification of the theory to exclude a higher-order term, which seemed to cause discrepancies between theoretical solutions and experimental data from two-dimensional and axisymmetric cases. Livesey & Laws (1973*b*) also produced axisymmetric velocity profiles using these curved screens. Dunn & Tavoularis (2007) revisited this type of method to combine theoretical and empirical information to produce shear flows through curved screens. Mean flows with approximately uniform shears and different shear rates were successfully generated in a water channel. The most obvious drawback of any method using gauze and wires is, as commented by Lawson (1968), that the turbulence characteristics cannot be varied once the wire is chosen, and it is therefore impossible to generate mean velocity and turbulence profiles independently.

The parallel wire method relies mostly on the spacing of the wires, and it is therefore hard to adjust the elements locally. Another type of shear generator was tested by Champagne, Harris & Corrsin (1970), where the authors used plates of 609.6 mm long, and 3.175 mm thick separated by 25.4 mm to form parallel channels with adjustable internal screens to control the local solidity. The same method was then used by many, e.g. Harris, Graham & Corrsin (1977); Tavoularis & Corrsin (1981), Karnik & Tavoularis (1987), Rohr *et al.* (1988), Garg & Warhaft (1998), Nedić & Tavoularis (2016), with different configurations such as the size of internal grid size, and the separation distance of the plates. A honeycomb with uniform cell diameter but varying lengths in the streamwise direction was also tested by Rose (1970) to generate shear flows. This author studied the combination of such a honeycomb and a grid placed downstream with different sizes and geometries, and the downstream grid was shown to reduce the mean shear rate. Richards & Morton (1976) produced a quadratic mean velocity profile using such a honeycomb and grid combination. Mulhearn & Luxton (1975) used a similar set-up where a non-uniform parallel rod grid was placed upstream of the honeycomb with uniform length to produce a uniform sheared flow. Note that no relation between the shear flow and the geometry of the set-up was concluded from these parallel plate methods since all of them were tuned by trial and error. Even though they offer the possibility of local adjustments of the device, which is an improvement of the previous method,

https://doi.org/10.1017/jfm.2018.387 Published online by Cambridge University Press

they lack theoretical support to relate the grid geometry to the generated shear flow. Experiments involving extremely high shear rates, e.g. $\partial U/\partial y > 400\ \mathrm{s}^{-1}$ (where U is the mean velocity and y is the shear direction, see Souza, Nguyen & Tavoularis 1995), are excluded from our discussion. We also mention that there have been studies on the Couette flow generated by moving walls as a means to produce velocity profiles (Coles 1965; Tillmark & Alfredsson 1992; Bottin *et al.* 1998), yet the fundamental idea is different from this study, and the discussion on these studies is therefore not elaborated here.

The active grid proposed by Makita (1991) and the subsequent works (see e.g. Mydlarski & Warhaft 1996; Shen & Warhaft 2000; Cekli & van de Water 2010; Knebel, Kittel & Peinke 2011; Hearst & Ganapathisubramani 2017) provided another option to tailor turbulent flows. It is typically used to produce a higher turbulence level, and is sometimes combined with other passive devices to produce shear flows (see e.g. Zhu *et al.* 2006; Bai, Meneveau & Katz 2012; Thormann & Meneveau 2015). Hearst & Ganapathisubramani (2017) proposed the possibility to obtain independent control of the mean flow and turbulence intensity using the active grid. They produced shear flows with small shear rates ranging approximately 6.25–12.5 s^{-1} over a physical domain of 0.32 m and generated profiles of varying turbulence intensity and high Reynolds numbers. Hearst & Ganapathisubramani (2017) claimed that such shear flows would be directly applicable in wind turbine experiments. Amongst many advantages, the methodology of active grid-generated turbulence, however, is rather costly to implement, and the establishment of control protocols is largely empirical. The work of Hearst & Ganapathisubramani (2017) did not provide quantitative relations between the control parameters and the turbulence characteristics. Therefore we explore the possibility of a type of passive grid design for producing desired turbulence fields. This idea is also supported by the conclusion of Roach (1987) that the turbulence energy scales on the bar dimensions rather than the mesh size, which suggests that it is possible to manipulate the turbulence intensity through the design of the grid bars.

In this paper we attempt to combine the known methodology for producing mean shear with fractal/multiscale ways to produce scalable high turbulence intensities at the same time. For this reason, we refer to the studies of fractal grids proposed by Hurst & Vassilicos (2007), especially the space filling fractal square grids (e.g. Seoud & Vassilicos 2007; Mazellier & Vassilicos 2010; Valente & Vassilicos 2011; Gomes-Fernandes, Ganapathisubramani & Vassilicos 2012; Hearst & Lavoie 2014; Isaza, Salazar & Warhaft 2014) where the development of downstream turbulence is quantitatively related to the grid geometries. These fractal square grids are characterized by repeated square patterns of different sizes, and the blockage ratio is usually small ($\sigma \approx 25$–$30\,\%$). Detailed descriptions can be found in Seoud & Vassilicos (2007), Hurst & Vassilicos (2007), Mazellier & Vassilicos (2010).

Mazellier & Vassilicos (2010) studied the fractal-generated turbulence, and proposed the wake interaction length scale $x_* = g_0^2/w_0$, where g_0 is the largest length of the bars, and w_0 is the largest width. This scaling relation succeeded in collapsing both the centreline mean velocity and turbulence intensity profiles. The peak of the turbulence intensity was found at $x_{peak} \approx 0.45x_*$ with a maximum level of approximately $15\,\%$ U_∞. Later, Gomes-Fernandes *et al.* (2012) extended the study to include the effects of the aspect ratio of the bars and the free-stream turbulence level, and proposed the improved scaling relation $x_*^{peak} = 0.21g_0^2/(\alpha C_D w_0)$, where $\alpha = 0.231$ is a constant associated with the wake development for flows with minimal inlet free-stream turbulence intensity, and C_D is the drag coefficient of the bar. This x_*^{peak} provided better collapse of the streamwise turbulence intensity profiles from different grids, and

https://doi.org/10.1017/jfm.2018.387 Published online by Cambridge University Press

was taken to be an important parameter for designing the grids. Gomes-Fernandes *et al.* (2012) also proposed a scaling relation for the turbulence intensity levels, and the scaled turbulence intensity $(u'/U_\infty)\beta(C_D w_0/x_*^{peak})^{-1/2}$ (where $\beta = 2.88$ is a constant for laminar free stream, and U_∞ is the inlet free-stream velocity) collapsed six different inlet conditions as a function of x/x_*^{peak}. These scalings are adapted and discussed further in the design process of our new multiscale inhomogeneous grids.

1.2. *Shear flow characteristics*

The development of turbulence intensity in a grid-generated shear flow was perhaps first discussed by Rose (1966). The author generated a homogeneous turbulent shear flow with a mean shear gradient $S = \partial U/\partial y = 13.69\ \mathrm{s}^{-1}$ which retained its value up to $x/H = 9.76$, where H is the height of the grid. The turbulence intensities u' and v' were found to be nearly uniform along the mean shear direction y at $x/H = 1.33$, but the two edges were affected by the growing boundary layer on the tunnel wall and the turbulent intensities were significantly larger on the sides. Along the centreline, u' and v' decayed to levels $u'/U_c = 1.2\,\%$ and $v'/U_c = 0.8\,\%$, where U_c is the centreline mean streamwise velocity.

Champagne *et al.* (1970) produced a mean shear rate $S = 12.9\ \mathrm{s}^{-1}$ using the parallel plates with internal screens, and the shear was maintained in the range $x/H = 3$–9.5. The centreline turbulence intensity u'/U_c reached a constant value of $1.8\,\%$ after $x/H = 6.5$. Rose (1970) created shear flows using different combinations of honeycomb and wire grids, and produced mean shear rates in the range $S = 6$–$12\ \mathrm{s}^{-1}$. The streamwise turbulence intensity levels u'/U_c in the range $x/H = 7$–9 were shown to be constant, and their values increased from 0.2 to $2\,\%$ with increasing grid size.

Harris *et al.* (1977) improved on the work of Champagne *et al.* (1970) and produced a larger mean shear rate $S = 44\ \mathrm{s}^{-1}$ which remained almost constant up to a dimensionless time scale $\tau^* = 12$, where $\tau^* \equiv (x/U_c)(\partial U/\partial y)$. Their hot-wire results showed a larger normalized turbulence intensity compared to that in Champagne *et al.* (1970), and the turbulence intensities were found to grow with streamwise distance after $\tau^* \approx 4$. The growth of turbulence intensities along the streamwise direction was then studied by Rohr *et al.* (1988) for several cases, where the grid size, centreline velocity and mean shear rate were varied. The results clearly showed a region of increasing streamwise turbulence intensity u'/U_c. The critical point τ_c^*, where u'/U_c reached its minimum was studied by several authors, and interestingly the turbulence intensity beyond τ_c^* remained constant in some cases (e.g. Rose 1966; Champagne *et al.* 1970; Rose 1970), but grew in some others (e.g. Harris *et al.* 1977; Tavoularis & Corrsin 1981; Rohr *et al.* 1988; Nedić & Tavoularis 2016). For the cases where u'/U_c stayed constant, the development was fairly fast, reaching constant values at $\tau_c^* = 1.6$–3, whereas for those cases exhibiting growing u'/U_c the critical point was observed at roughly $\tau_c^* = 4$–5. Tavoularis & Karnik (1989) studied this more systematically and suggested that when the shear is weak, i.e. $\epsilon/P \sim 1$, the turbulence kinetic energy will remain constant after τ_c^*, whereas for strong shears, where $\epsilon/P < 1$, the turbulence kinetic energy will grow exponentially after τ_c^*.

Regarding the Taylor microscale λ, Harris *et al.* (1977) reported a constant value of λ in the range $\tau^* = 6$–11, with $S = 44\ \mathrm{s}^{-1}$. Rohr *et al.* (1988) also reported a constant λ from $\tau^* = 6$ with approximately $S = 1\ \mathrm{s}^{-1}$, while Tavoularis & Karnik (1989) showed in their experiments that λ approached a constant value at $\tau^* \approx 16$ for mean shear rates $S = 44\ \mathrm{s}^{-1}$ and $84\ \mathrm{s}^{-1}$. More recently Nedić & Tavoularis (2016) reported a constant λ downstream of $\tau^* \approx 9.25$ in a uniformly sheared flow with $S = 62\ \mathrm{s}^{-1}$. By comparing

https://doi.org/10.1017/jfm.2018.387 Published online by Cambridge University Press

the results from Harris *et al.* (1977) and Rohr *et al.* (1988), it can be concluded that the location where λ stops growing is not only a function of the mean shear rate, but other factors as well.

In terms of integral length scales, all of the previous results showed monotonic increases with streamwise distance. Results by Nedić & Tavoularis (2016) also showed a decrease of growth rate of the longitudinal integral length scale $L_{uu,x}$ beyond approximately $\tau^* = 9$. Some studies reported relations between longitudinal and transverse integral length scales such that $L_{uu,x} = 2L_{uu,y}$, indicating a large scale isotropy (e.g. Rose 1966; Champagne *et al.* 1970; Harris *et al.* 1977). Further discussion on length scales is provided in § 3.5.1.

1.3. *Objectives*

The main objective of the present work is to design and test a new class of turbulence generating grids to find the possibility to scale the mean velocity and turbulence intensity profiles to the geometry of the grid, which might provide the ability to produce desired mean velocity and near-field turbulence intensity profiles simultaneously. For the current discussion, only weakly sheared turbulence is considered with shear rates ranging from 0 to 5 s^{-1}, comparable to the cases studied by Hearst & Ganapathisubramani (2017) using active grids. Such weakly sheared flows can be used to represent a certain part of a shear layer, and therefore are practical in various wind tunnel testing scenarios. Even though homogeneous shear flows are important as a subject of fundamental interest, they are not the subject of the present study. In this paper, we attempt to establish relations between the geometry and different turbulent flow profiles. Homogeneous turbulent shear flows could be considered in a future study, which might attempt to apply our method of flow generation.

In the following context, the details of the grid geometry are given first. It is then shown that the mean velocity profiles predicted using the mean velocity model derived from Taylor *et al.* (1949) and McCarthy (1964) are in good agreement with our experimental data. By modifying the grid thickness the aspect ratio of the grid bars are changed, and consequently the drag coefficients. The effect of drag coefficient on the local mean velocity gradient is discussed. The turbulence intensity profiles at given streamwise location x are found to scale with the geometry of the grid bars. The scaling relations between the turbulence field and the geometry of the grid might be used in the future to generate other types of turbulence flows of interest. A general procedure of the grid design method is proposed in § 3.3.

Results on the evolution of turbulence intensities and length scales are also presented, and finally a simplified model is proposed to describe the downstream development of the turbulence field generated by these grids. This model allows description of the turbulence field using just one measurement of vertical profile close to the grid and one centreline profile along the streamwise direction.

2. Experiments

2.1. *Facility*

All experiments were conducted in the $3' \times 3'$ closed loop wind tunnel in the Aeronautics Department at Imperial College London. The test section has a cross-sectional area of 0.91×0.91 m, and a measurable length of 4.2 m. The flow goes through a set of perforated screens and a 9:1 contraction before reaching

https://doi.org/10.1017/jfm.2018.387 Published online by Cambridge University Press

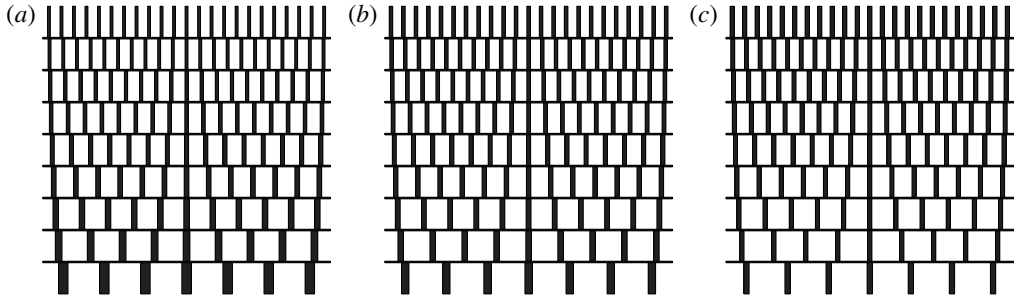


FIGURE 1. Schematic sketch of (*a*) grid 1, (*b*) grid 2 and (*c*) grid 3, respectively, in the z–y (horizontal–vertical) plane with $N = 9$ layers numbered from bottom to top as $n = 1, 2, \ldots, N$.

H, W	External height and width of grid
D	Thickness of the original grid (in x), and the horizontal supporting bars
N	Number of layers
h_n	Height of layer n
σ_n	Blockage ratio of layer n
c_n	Number of vertical bars in layer n
w_n	Width of the vertical bars (in z) in layer n
g_n	Distance between two adjacent vertical bars in layer n
d_n	Thickness of the vertical bars (in x) in layer n
a_n	Aspect ratio of the vertical bars, defined as $a_n = d_n/w_n$, in layer n
t_b	Width of horizontal bars (in y)

TABLE 1. Design parameters of multiscale shear grids.

the test section. The background turbulence intensity without the grid was measured to be $\sim 0.1\,\%$ at $U_\infty = 10$ ms^{-1}. A computer controlled traversing system is mounted on top of the working section, allowing movements in all three directions. The origin of the coordinate system is set at the bottom of the grid on the windward side.

2.2. *Grid design*

In this section we outline the design principles of our new multiscale grids. A schematic sketch is given in figure 1. Three such grids were made for the current investigation producing flows with different shear rates and different turbulence profiles, even though the geometries are very similar. The first grid was designed to generate a turbulent flow without mean shear, and a non-uniform turbulence intensity, while the other two were designed to generate turbulent flows with gradients in both mean velocity and turbulence intensity. The grids are numbered in order of increasing shear rates. They were laser cut in acrylic with a uniform thickness (in the x direction) of $D = 10$ mm.

There are several parameters involved in the design process, and a summary is given in table 1. The external height H and width W of the grid are determined by the dimensions of the wind tunnel test section in the y and z directions, respectively. For the current study we have $H = W = 0.91$ m. The number N of horizontal layers is chosen to be $N = 9$ for all three grids in the current study. This number can be

https://doi.org/10.1017/jfm.2018.387 Published online by Cambridge University Press

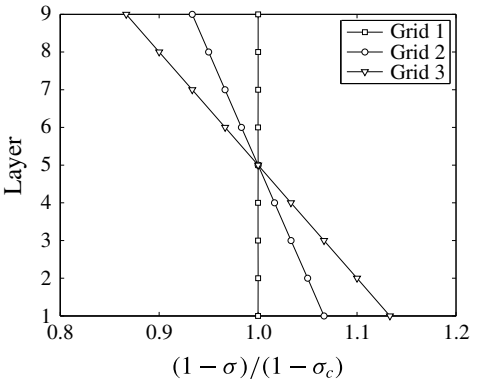


FIGURE 2. Profiles of $(1-\sigma)/(1-\sigma_c)$ for grid 1, 2 and 3, where σ_c is the blockage ratio at layer 5, the centre of the grid, i.e. $\sigma_c = \sigma_5$.

increased to obtain finer control over the local velocity gradient. The height of each layer h_n is set here to be $h_n = \text{constant} = 101.67$ mm. There are also eight horizontal supporting bars. Their width (in the y direction) for the present grids is $t_b = 5$ mm, and an aspect ratio of $D/t_b = 2$ was achieved to minimize the wake shed from them.

The most important parameters for the design of the mean flow profile are the blockage ratios σ_n of each layer. The normalized blockage ratio profiles for each grid are given in figure 2. The mean blockage ratio $(\sigma_1 + \sigma_2 + \cdots + \sigma_n)/N$ (with $N = 9$ here) was set to 25 % for all three grids, while the maximum local blockage ratio was set as $\sigma_9 = \sigma_{max} = 35\,\%$ to avoid flow recirculation. This is consistent with the observations of Rose (1966), who limited the maximum local solidity to $\sigma_{max} = 40\,\%$ for this reason.

While the blockage profile controls the mean velocity of the flow, the lateral widths and spacing of the vertical bars in each layer of the grid are tailored to vary the wake interaction mechanisms in order to generate different turbulence characteristics. Three parameters are introduced here, namely c_n the number of vertical bars, w_n the lateral width of each individual bar and a_n the aspect ratio of the bars (defined as $a_n = d_n/w_n$). Note that since the thickness of the original grid is constant, i.e. $d_n = D = 10$ mm, a_n varies with vertical bar width w_n and the drag coefficient C_D of each bar therefore varies with n, which affects the wake characteristics. The number of bars for each layer is set to be $c_n = 2(n + M) + 1$ for $n = 1, 2, \ldots, N$, where $M = 2$ is a control parameter for the current grids. The width of the bars are calculated from

$$w_n = \begin{cases} \dfrac{W}{c_n}\left(\dfrac{h_n\sigma_n - t_b}{h_n - t_b}\right), & n = 2, 3, \ldots, N-1 \\ \dfrac{W}{c_n}\left(\dfrac{h_n\sigma_n - 0.5t_b}{h_n - 0.5t_b}\right), & n = 1, N. \end{cases} \tag{2.1}$$

As shown in figure 1, there are no horizontal bars at the top and bottom edges of the grids, and the area is distributed in the vertical bars at layer 1 and N using the second equation in (2.1). At each layer, the vertical bars are evenly separated by a distance g_n, and are placed symmetrically about $z = 0$.

Note that the uniform thickness of the original grid inevitably causes variable aspect ratios $a_n = d_n/w_n$ of the vertical bars as the width w_n varies. Figure 3(*a*) gives the

https://doi.org/10.1017/jfm.2018.387 Published online by Cambridge University Press

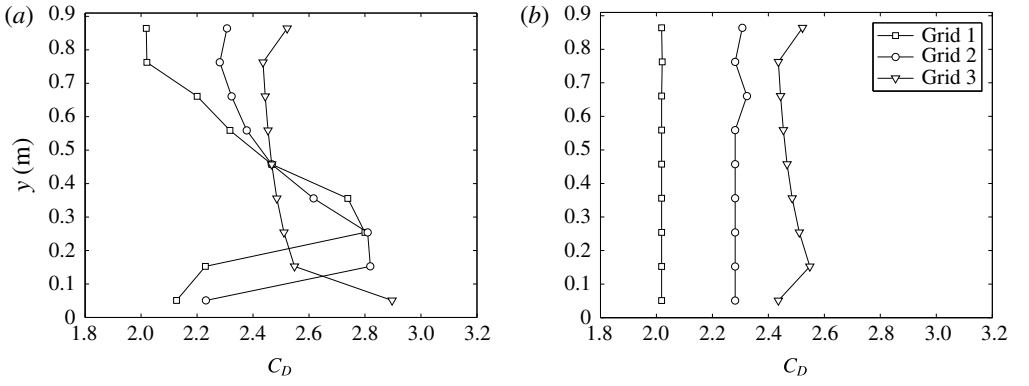


FIGURE 3. Vertical drag coefficient profiles of (*a*) original grids with uniform thickness $D = 10$ mm, and (*b*) modified grids with variable thickness but uniform aspect ratio.

C_D profiles of the three grids evaluated using the relation between C_D and the aspect ratio a_n given by Bearman & Trueman (1972). The Reynolds number of the vertical bars with $U_\infty = 10$ ms^{-1} is within the range 6000–20 000, and the Reynolds number dependence of the drag coefficient C_D is therefore negligible. The grids were also modified by attaching blocks behind the vertical bars to achieve a uniform aspect ratio a_n by effectively varying d_n, and hence a uniform C_D. Due to the dimensions of the vertical bars, the aspect ratio is set equal to that of the eighth layer a_8. For grid 3, however, the modification was only applied to the bottom layer $n = 1$, because the additional thicknesses to be attached to the other layers were all smaller than 1 mm, and therefore difficult to manufacture. The drag coefficient profiles after the modification are given in figure 3(*b*).

Now if we refer to the scalings for grid-generated turbulence proposed by Vassilicos and colleagues as outlined in the introduction, we can calculate the wake interaction length scale for each layer n as $x_{*,n}^{peak} = 0.21 g_n^2/(\alpha C_D w_n)$ by substituting $L_0 = g_n$ and $t_0 = w_n$ in their original equation (Gomes-Fernandes *et al.* 2012). The results for the original and modified grids are plotted in figure 4(*a*,*b*), respectively. It can be observed that the variation of $x_{*,n}^{peak}$ with n becomes much more smooth due to the modification of C_D, and the maximum x_*^{peak} is approximately $x = 0.38$ m from the grid. From the results of Gomes-Fernandes *et al.* (2012), where the turbulence intensity profiles from several experiments and different grids collapsed against x/x_*^{peak}, it can be expected (see Gomes-Fernandes *et al.* 2012) that the streamwise turbulence intensity at level n scales with $(x_*^{peak})^{1/2}$. Further results and discussions on this scaling relation are presented in § 3.2.

2.3. *Experimental set-up and method*

The tunnel inlet velocity U_∞ was monitored using a Furness Controls FCO510 micromanometer which measures the static pressure head across the contraction and the temperature. The inlet velocity U_∞ was maintained using a proportional–integral–derivative (PID) controller to be within $\pm 1.5\,\%$ of 10 m s^{-1} for all data sets in the current study. Only one inlet velocity is tested as previous studies showed that the turbulence statistics produced by grid with square bars is independent of the Reynolds number (see Roach 1987). Data were then acquired with MATLAB, using a 16-Bit National Instruments NI-6229(USB) board. Instantaneous velocity signals

https://doi.org/10.1017/jfm.2018.387 Published online by Cambridge University Press

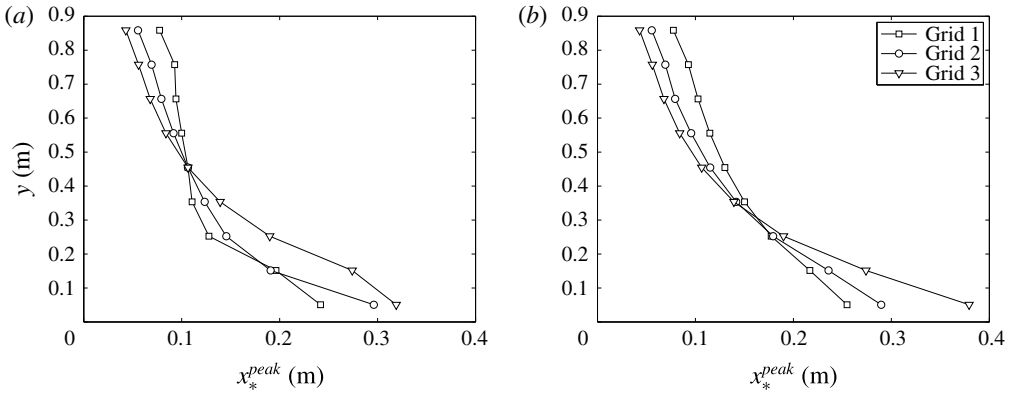


FIGURE 4. The wake interaction length scale $x_{*,n}^{peak}$ for (*a*) original grids with uniform thickness $D = 10$ mm, and (*b*) modified grids with variable thickness but uniform aspect ratio.

were measured using an in-house etched platinum Wollaston cross-wire powered by a Dantec Streamline CTA system. The diameter of the wire was $d_w = 5$ μm with length to diameter ratio approximately 200. Resolution of the wire are estimated to be $l/\eta = 2.6$–7.2, where the Kolmogorov length scale η was estimated using $\eta = (\nu^3/\epsilon)^{1/4}$. To calculate ϵ, we compute $\epsilon_* = 15\nu\overline{(\partial u/\partial x)^2}$ and $\epsilon_{**} = 3\nu\overline{(\partial u/\partial x)^2} + 6\nu\overline{(\partial v/\partial x)^2}$, and then use the average $\epsilon = (\epsilon_* + \epsilon_{**})/2$ in this paper.

The hot-wire probe was mounted on a servo motor to allow accurate control of the pitching angles. It was calibrated at the beginning and end of every data set acquired using the look-up table method for five velocities from 3 to 19 m s^{-1} and seven angles ranging from $-27°$ to $27°$. The temperature was monitored during acquisitions, and the data were discarded if temperature variation $\Delta T_a = T_{a,max} - T_{a,min}$ was larger than 0.1 °C. Two packets of $t_s = 300$ s samples were acquired to ensure convergence in mean statistics. Longer samples ($t_s > 300$ s) were not possible as the drift of the ambient temperature during acquisition will add artificial large scale variation. The acquisition rate was 125 kHz, and a low-pass filter of 30 kHz was applied before the data were recorded to avoid aliasing. The data were also low-pass filtered before the processing to eliminate high frequency noise.

To calculate the longitudinal integral length scales $L_{uu,x}$, one either integrates the correlation function R_{uu} or uses the streamwise turbulence kinetic energy spectrum $E_{11}(k)$ as $L_{uu,x} = \pi E_{11}(0)/(2u'^2)$ (see Tennekes & Lumley 1972). It is noted that the spectrum and the correlation function is a Fourier pair. Yet the zero frequency asymptote of the digitally acquired spectrum has large uncertainty and the integral length scale is usually extrapolated from a number of the low frequency spectral estimates. For the other method, the integral of the correlation function cannot be taken to infinity, and thus an upper limit of the integration has to be chosen. Moreover, this upper limit of the integration is not well defined, and the integration result using different upper limit varies as large as 20 % (O'Neill *et al.* 2004). We therefore seek a way to correct the lower frequency range of the spectra before estimating the longitudinal integral length scale $L_{uu,x}$.

Several models have been proposed for estimating the power spectra density $E(k)$, and the most frequently used is the von Kármán model, which can be written in a

https://doi.org/10.1017/jfm.2018.387 Published online by Cambridge University Press

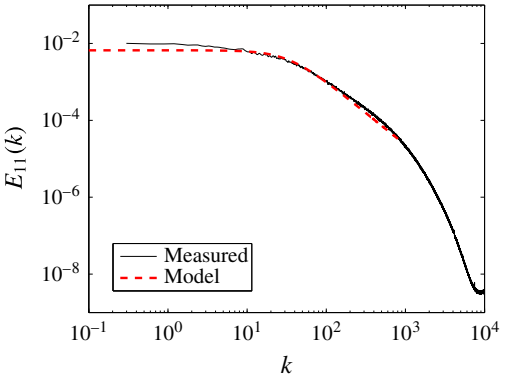


FIGURE 5. (Colour online) Example spectrum for grid 2 at centreline $x = 0.83$ m.

one-dimensional form as

$$E_{11}(k) = \frac{2u'^2 L_{uu,x}}{\pi} \frac{1}{\{1 + [kL_{uu,x}B(1/2,\, 1/3)/\pi]^2\}^{5/6}}, \tag{2.2}$$

where u' is the turbulence intensity, k is the wavenumber defined as $k = 2\pi f/U_\infty$ (f is the frequency in time) and B is the beta function related to the Γ function by $B(1/2,\, 1/3) = \Gamma(1/2)\Gamma(1/3)/\Gamma(5/6)$. In practice, we first take the average of the spectra of two packets of data, and use (2.2) to fit the data in a least square sense. One example is given in figure 5, where it is shown that the small wavenumber range of the original spectrum (black) is slightly tilted upward leading to a larger value of $E_{11}(0)$. This effect is most obvious at locations close to the grid where $x = 0.83$ m, but much less further downstream. This method is used in § 3.5.1 to correct the lower frequency part of the spectrum.

It is acknowledged that most spectrum models have potential flaws in the low frequency range. There have been other models, e.g. Wilson (1998), where a two parameter spectrum model is proposed that allows more freedom in fitting the inertial range and inertial sub-range of the spectrum. However, that model works well only in turbulent flows with sufficiently large Reynolds numbers that has more decades of $-5/3$ slope, otherwise the extra parameter causes large uncertainties in the fitted spectrum. For the current study, the Reynolds number is moderate so that models such as Wilson's (1998) are not considered.

3. Results

3.1. *Mean velocity*

Before showing the measured vertical mean velocity profiles produced by the grids, we refer to previous works that used wire gauzes to produce non-uniform mean flow profiles. Following Taylor *et al.* (1949), McCarthy (1964), the streamwise velocity near the grid (upstream denoted by '-0' and downstream denoted by '$+0$') can be related by

$$\frac{U_{+0}}{U_{-0}} = \frac{1 + \alpha_n - \alpha_n K_n}{1 + \alpha_n + K_n}, \tag{3.1}$$

https://doi.org/10.1017/jfm.2018.387 Published online by Cambridge University Press

where the subscript n denotes the layer number, α_n is the refraction coefficient at layer n and K_n is the resistance coefficient of the grid, which can be calculated from

$$K_n = \frac{r\sigma_n}{(1-\sigma_n)^2}, \tag{3.2}$$

where σ_n is the local blockage ratio of the grid at layer n, and r is an empirical constant in the range $0.65 < r < 1$ (see McCarthy 1964). Cornell (1958) reported a constant value of $r = 0.7$ for the range $2000 < Re < 40\,000$. For the current grids, the Reynolds number based on $U_\infty = 10$ ms^{-1} and bar width w is calculated to be in the range 6000–20 000. The value of r is therefore chosen to be $r = 0.7$ in this work. Although there are other ways to calculate the value of K_n (as summarized in Karnik & Tavoularis 1987), (3.2) seems to give the best result at least for the current cases.

Finally, an empirical expression of the refraction coefficient at layer n of the grid is given in both Taylor *et al.* (1949) and McCarthy (1964) as

$$\alpha_n = 1.1(1+K_n)^{-1/2}, \tag{3.3}$$

which was also concluded by these authors to be insensitive to Reynolds number.

In figure 6(*a*), we present the vertical profiles of streamwise velocity U measured at $x = 0.83$ m and $x = 4.13$ m for the original grids (i.e. with non-uniform C_D as shown in figure 3*a*), together with the profiles calculated using (3.1)–(3.3) with $r = 0.7$. Measurements were taken from the middle of the second layer up to the middle of the seventh layer. Note that there was no trial and error involved in generating the velocity profiles. The normalized profiles U/U_c are presented because the measured incoming velocity (at the beginning of the test section) is different from U_{-0} in (3.1) by a constant factor.

A wave-like deviation of the mean velocity profiles across these original grids is observed, especially for grid 1 where the variation of C_D is the largest. The non-uniform drag coefficient C_D of the vertical bars in the grid at each layer effectively modifies the local blockage ratio and consequently the local mean velocity. Other than that, the shapes of the velocity profiles generally follow the model, and the shape of the mean profiles is maintained within the measurement range of approximately $x/H =$ 1–4.5. This is consistent with previous conclusions from the parallel wire-generated or plate-generated shear flows (e.g. Rose 1966; Champagne *et al.* 1970; Shen & Warhaft 2000).

The measurements behind the modified grids, as described in § 2.2, are given in figure 6(*b*). It is obvious that both grids 1 and 2 collapse better with the predicted profile when the non-uniformity of C_D is eliminated. This shows that the drag coefficient indeed affects the mean velocity profile quite significantly. As for grid 3, the only modified layer is the bottom one, which is outside the measurement range, and thus the mean velocity profiles of the original and modified grids are almost identical. Again, these results are obtained without trial and error, suggesting that (3.1)–(3.3) can serve as a guideline for bespoke design of desired mean velocity profiles using our proposed inhomogeneous multiscale geometries.

For the modified grids, the shape of the mean profiles is also maintained, in fact better than that for the original grids. The absolute values of the averaged mean shear rate $|\overline{\partial U/\partial y}|$ are 0.29 s^{-1}, 2.97 s^{-1} and 4.99 s^{-1} for grids 1, 2 and 3, respectively. These shear rates are rather small compared to those of Champagne *et al.* (1970) and Harris *et al.* (1977). Nevertheless, higher shear rates could in theory be achieved by

https://doi.org/10.1017/jfm.2018.387 Published online by Cambridge University Press

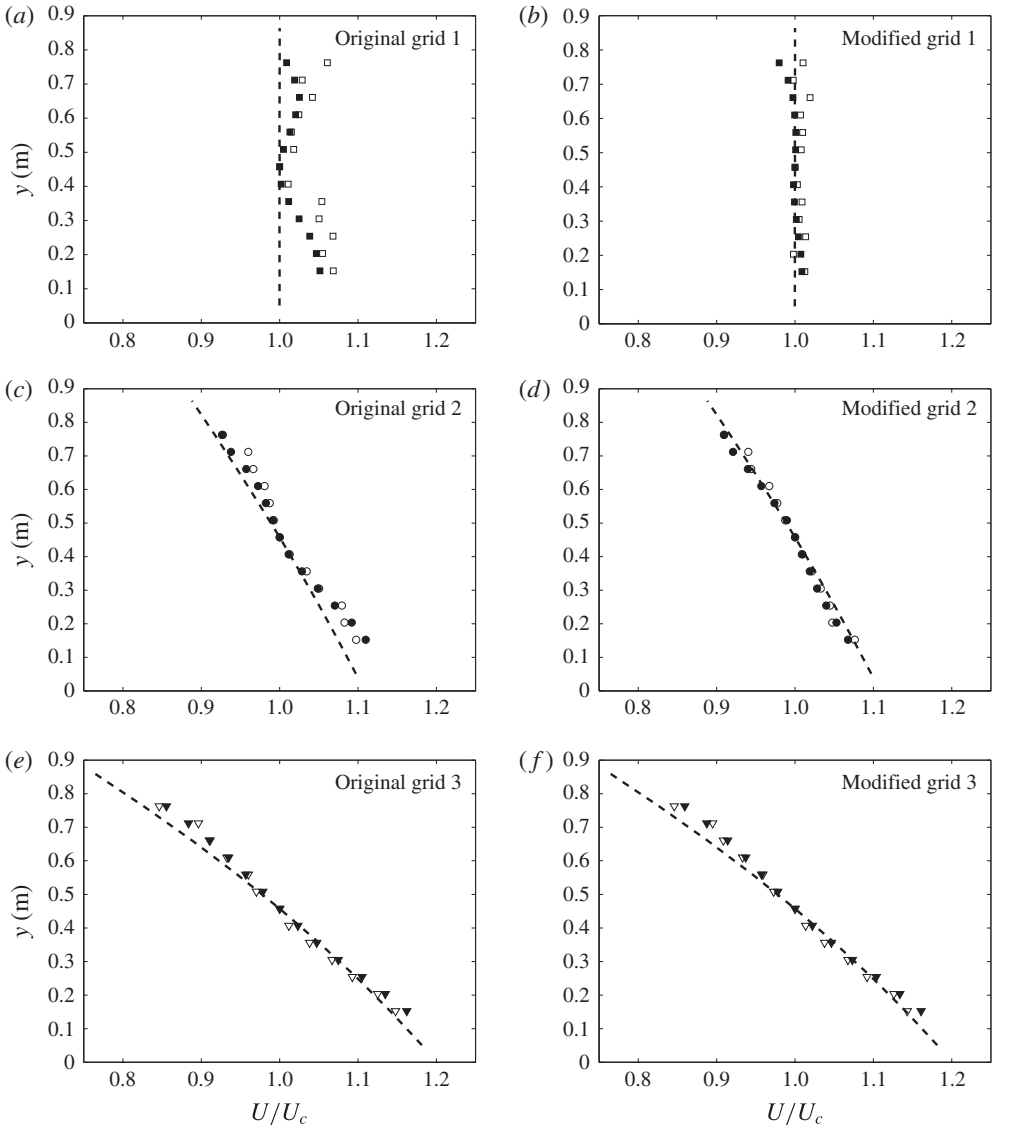


FIGURE 6. Vertical profiles of the normalized streamwise velocity U/U_c (symbols) and equation (3.1) (dashed lines) for original grids (with uniform thickness $D = 10$ mm) and modified grids (with variable thickness but uniform aspect ratio). Empty symbols, $x = 0.83$ m; filled symbols, $x = 4.13$ m.

increasing the gradient of blockage ratio σ_n of the grid, as long as σ_{max} does not exceed the limit required to avoid recirculations, e.g. $\sigma_{max} = 35\,\%$ for the current case.

Figure 7 shows the mean velocity profiles along the streamwise direction downstream of the modified grids measured at $y = 0.25$ m, $y = 0.46$ m and $y = 0.66$ m with streamwise step of $\Delta x = 0.3$ m. The difference between the profiles at each y position indicates the shear rate of the flow. The linear fit of the centreline profiles along x gives slopes of 0.0092, -0.043, and -0.067, respectively, and it is concluded that the mean velocity is roughly constant along the streamwise direction. This also

https://doi.org/10.1017/jfm.2018.387 Published online by Cambridge University Press

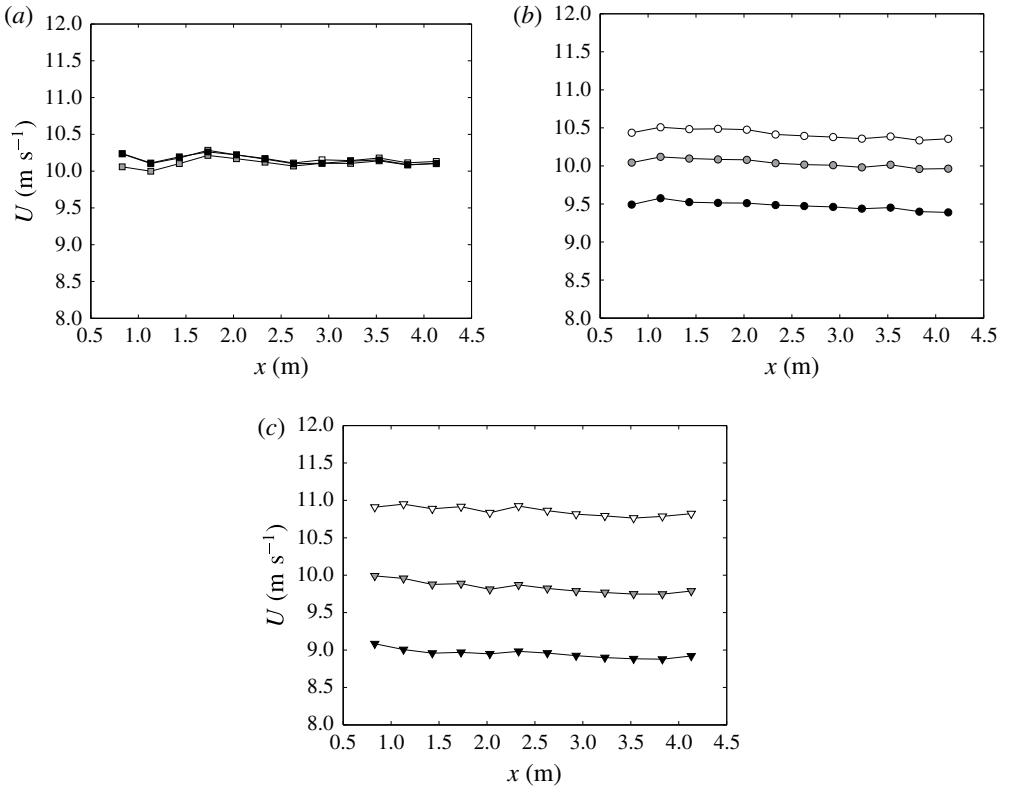


FIGURE 7. Streamwise velocity profiles for modified (*a*) grid 1, (*b*) grid 2 and (*c*) grid 3, at $y = 0.25$ m (white), $y = 0.46$ m (grey) and $y = 0.66$ m (black).

coincides with the velocity profiles observed in figure 6. In the rest of the paper, only modified grids are discussed to exclude the unwanted velocity variations caused by the non-uniform C_D of the original grids.

3.2. *Turbulence intensities*

To begin this section, we present the turbulence intensities measured at different streamwise locations. The profiles of u'/U_∞ and v'/U_∞ are plotted along the centreline at $y = 0.46$ m in figure 8(*a*). The decay of both u' and v' is obvious, and the value of v' is always smaller than u' for each individual grid at all locations, and approximately follows $u'^2 = 2v'^2$, which is consistent with many previous observations in various turbulent shear flows (e.g. Champagne *et al.* 1970; Tavoularis & Corrsin 1981; Garg & Warhaft 1998; Vanderwel & Tavoularis 2014). The averaged ratio of u'^2/v'^2 throughout all x locations along the centreline for grid 1, 2, 3 is 1.93, 1.90, 2.07, respectively. The value of u'/U_∞ for all grids at different y locations drops from approximately 7 to 2 % along the streamwise direction, and it seems for grid 3 that the streamwise turbulence level u' remains higher than the others. This might be explained by the higher drag coefficient C_D as shown in figure 3, and the larger mean shear rate of grid 3, which generates turbulence intensity through production and keeps the turbulence level higher than the other grids.

In figure 8(*b*), we plot u'/U_∞ and v'/U_∞ along the shear direction y at $x = 0.83$ m. Both components of the turbulence profiles show a gradient along the shear direction,

https://doi.org/10.1017/jfm.2018.387 Published online by Cambridge University Press

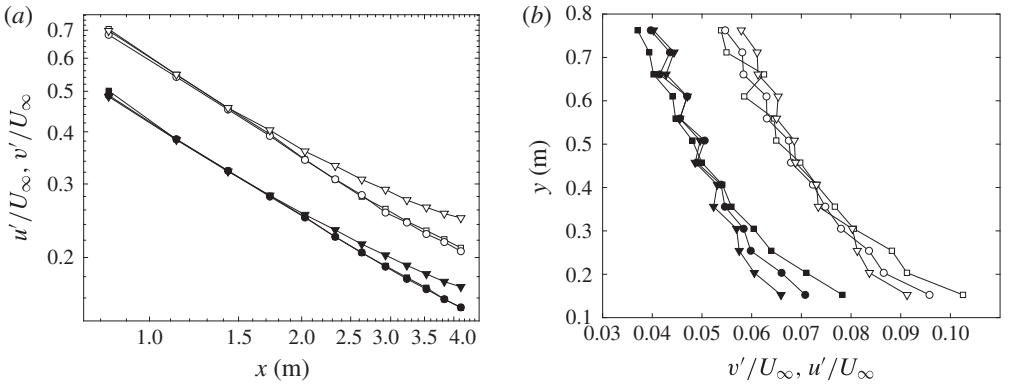


FIGURE 8. Profiles of turbulence intensity u'/U_∞ (empty symbols), v'/U_∞ (filled symbols) along (*a*) streamwise direction x at the centreline $y = 0.46$ m, and (*b*) vertical direction at $x = 0.83$ m for grid 1 (square), grid 2 (circle) and grid 3 (triangle).

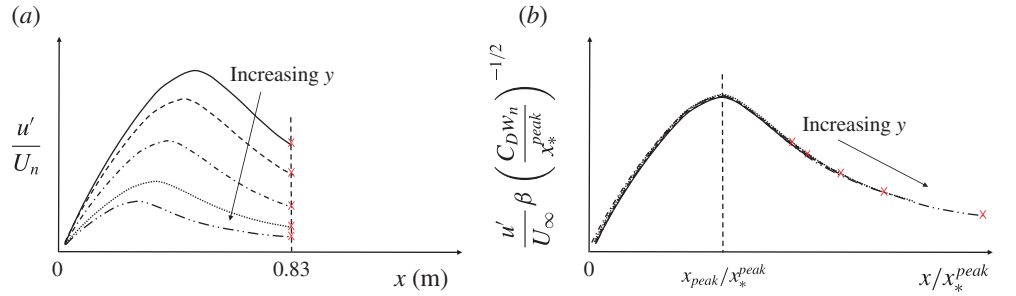


FIGURE 9. (Colour online) Schematic sketch to show the scaling method of the normalized turbulence intensities along y. Different line types represent the streamwise turbulence intensity developments behind different layers of the grid.

and the largest value of u'/U_∞ reaches above 10 % even at $x = 0.83$ m (or $x/H = 0.9$). This is quite large compared to conventional grid-generated turbulence, where the turbulence decays rapidly downstream of the grid, and it suggests that it is possible to increase the turbulence level using the vertical bars. This can be of practical importance for experiments that require large turbulence intensities at a distance downstream of the grid. From this point of view, it is desired to have a quantitative scaling relation for $u'(x, y)$.

To scale the turbulence intensity profiles $u'(y)$ at given x closely downstream of the grid, we refer to the work of Gomes-Fernandes *et al.* (2012) mentioned in the introduction. The streamwise turbulence intensity level therefore depends on the streamwise development of the turbulence behind each layer of the grid, as shown in figure 9(*a*), where the turbulence level and peak location varies from layer to layer. This peak location x_{peak} is different for different layers but scales with the wake interaction length scale x_*^{peak}, which is itself different at different layers n. The results of Gomes-Fernandes *et al.* (2012) also suggest that the turbulence intensity at the peak location can be collapsed in the form $(u'/U_n)\beta(C_D w_n/x_{*,n}^{peak})^{-1/2}$, where $\beta = 2.88$ is a constant corresponding to the wake development with laminar incoming flow condition, and U_n is the mean velocity at layer n. Figure 9(*b*) shows how the streamwise turbulence intensities $u'(x, y)/U_n$ can be collapsed.

https://doi.org/10.1017/jfm.2018.387 Published online by Cambridge University Press

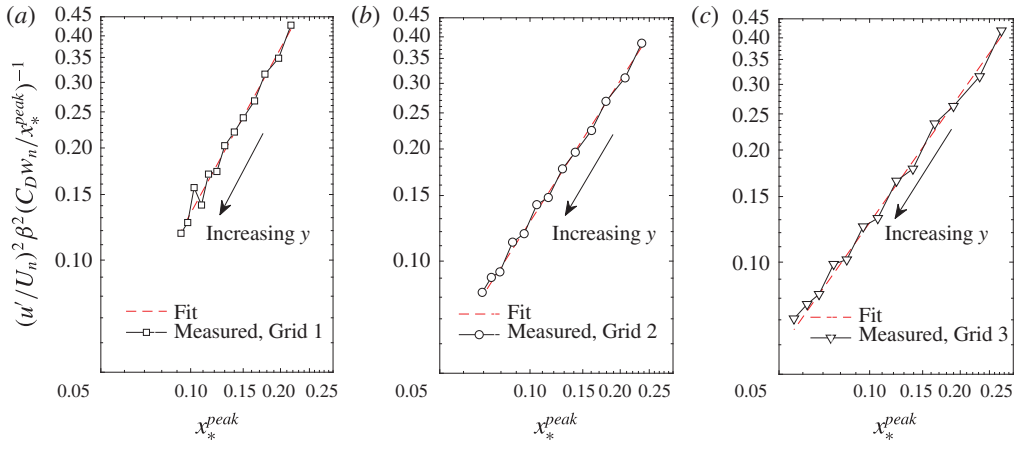


FIGURE 10. (Colour online) Scaling of the normalized turbulence intensity profiles $u'(y)$ measured at $x = 0.83$ m for (*a*) grid 1, (*b*) grid 2, (*c*) grid 3, respectively.

The current grids are designed such that the x_*^{peak} at all levels n are smaller than the first measurement location $x = 0.83$ m (see figure 4*b*), and all the data are therefore in the decay region $x/x_*^{peak} > 1$. We now attempt to use the scalings given in figure 9(*b*) to establish the y-profile of u' at $x = 0.83$ m.

For a streamwise location $x = x_m$, $(u'/U_n)\beta(C_Dw_n/x_{*,n}^{peak})^{-1/2}$ is a function of $x_m/x_{*,n}^{peak}$, where $x_{*,n}^{peak}$ varies along the y direction, as shown in figure 4. If we assume this function to be a power law, i.e. $(u'/U_n)^2\beta^2(C_Dw_n/x_{*,n}^{peak})^{-1} \sim (x_m/x_{*,n}^{peak})^b$, and fit our measurements of $u'(y)/U_n$ obtained at $x_m = 0.83$ m, we have $b = 1.47$, 1.26 and 1.14 for grids 1, 2 and 3, respectively. It can be observed in figure 10 that the fitted power law functions (dotted line) matches our measurements quite well, which quantitatively relates the downstream turbulence intensities with the geometry of the grid bars, i.e. C_D, w_n and g_n.

3.3. *A general grid design approach*

Based on the mean velocity model from § 3.1, and the turbulence intensity scaling from § 3.2. We now outline a possible procedure to design a grid to produce a flow with bespoke mean velocity and turbulence profiles.

First, the desired mean velocity profile $U_{target,n}$ is used as an input for (3.1)–(3.3) to solve for the blockage ratio σ_n, subject to $\sigma_n < 0.4$ to prevent recirculation. The average blockage ratio $\overline{\sigma_n}$ can be set to limit the pressure drop, which is $\overline{\sigma_n} = 0.25$ in this case. The problem can be solved by minimizing the error E_1 between the calculated value of U_n and the desired value $U_{target,n}$, which can be defined as $E_1 = \sum [U_n(\sigma_n) - U_{target,n}]^2$. Therefore the problem becomes to find

$$\left.\begin{array}{c}\min E_1(\sigma_n),\\ s.t. \sigma_n < 0.4, \overline{\sigma_n} = 0.25.\end{array}\right\} \tag{3.4}$$

For a uniform shear flow across the test section, the maximum mean shear rate one can achieve using this method depends on the physical size of the wind tunnel because the maximum blockage ratio is always limited by $\sigma \leqslant 0.4$, and the maximum variation of blockage ratio is $(\Delta\sigma)_{max} = 0.4$, which constrains the maximum variation of the

https://doi.org/10.1017/jfm.2018.387 Published online by Cambridge University Press

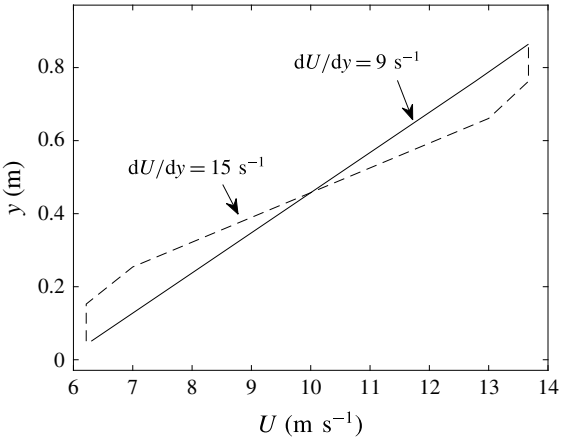


FIGURE 11. Calculated mean velocity profile to demonstrate the maximum mean shear rates achievable in a wind tunnel test section for the case of a uniform shear flow (solid line), and the case where only part of the test section is of interest (dashed line).

mean velocity ΔU. The mean shear rate $\mathrm{d}U/\mathrm{d}y$ will therefore become larger for a smaller physical domain. For example, for a uniform shear flow, the maximum mean shear rate could be achieved in the current facility (with test section of height $H = 0.91$ m) is approximately 9 s^{-1}, but higher mean shear rates could be achieved if only part of the test section is of interest, as demonstrated in figure 11.

Secondly, as shown in the previous section, at a streamwise location $x = x_m$, such that $x_m/x_*^{peak} > 1$, we have the scaling relation for the turbulence intensity profile along the y direction $u'(y)$ that $(u'/U_n)^2\beta^2(C_D w_n/x_{*,n}^{peak})^{-1} = a(x_m/x_{*,n}^{peak})^b$, where $\beta = 2.88$, and $C_D = 2.9$ for the current study. The turbulence intensity along the y direction can be therefore expressed as $u'/U_n = f_1(\beta, C_D, w_n, x_m, x_{*,n}^{peak}, a, b)$, where w_n is the width of the vertical bars at layer n, a and b are constants and $x_{*,n}^{peak}$ is the interaction length scale at layer n. The width of the grid bar w_n is determined by $w_n = f_2(\sigma_n, c_n, *)$ (where c_n is the number of the grid bars at layer n, and $*$ stands for other geometry details of the grid such as the overall width W and thickness of the horizontal bars, see (2.1)). Since the gap between adjacent vertical bars is defined by $g_n = W/c_n$, the interaction length scale $x_{*,n}^{peak} = 0.21g_n^2/(\alpha C_D w_n)$ (α is a constant characterizing the incoming flow condition) can be written as $x_{*,n}^{peak} = f_3(c_n, C_D, *)$. Finally, we have $u' = f(U_n, \beta, C_D, \sigma_n, c_n, x_m, a, b, *)$ with only three unknown variables, i.e. c_n, a and b. Given a target shape of the turbulence root-mean-square (r.m.s.) velocity profile $u'_{target,n}$, the solution of the problem might be solved by minimizing the error $E_2 = \sum [u' - u'_{target,n}]^2$. Note that the values of a and b cannot be determined analytically based on the current measurements, but their values seem to vary as a function of the mean shear rate S_n for a profile $u'(y)$ measured at a given streamwise location x_m, as shown in table 2. This table gives a possible range of the values of a and b, which might be used as a reference to set up the optimization problem. The problem becomes the minimization of

$$\left.\begin{array}{c} \min E_2(c_n, a, b, *), \\ s.t.\ a \in \mathcal{R},\ b \in \mathcal{R},\ a = f_a(S_n),\ b = f_b(S_n), \\ c_n \in \mathcal{Z},\ c_n \in [lb, ub], \end{array}\right\} \tag{3.5}$$

https://doi.org/10.1017/jfm.2018.387 Published online by Cambridge University Press

	S_n	a	b
Grid 1	0.29	3.93	1.47
Grid 2	2.97	2.32	1.26
Grid 3	4.99	1.78	1.14

TABLE 2. Variation of the fitting constants a and b at different mean shear rates, fitted using measurements at $x = 0.83$ m along the y direction.

where a and b are expressed as functions of the mean shear rate. The solution of the problem fully determines the geometry of the grid, and the shape of the target turbulence r.m.s. velocity profile $u'(y)$ could be achieved at a streamwise location $x_m/x_*^{peak} > 1$. The exact value of the turbulence intensity may not be achieved perfectly as yet, because a and b cannot be prescribed explicitly based on the current results. However, this procedure does ensure that the shape of the target profile is produced downstream of $x_{*,n}^{peak}$. The lower bound lb of c_n, is set to 2, which ensures that each layer has at least two vertical bars. The upper bound ub of c_n is determined using (2.1) and varies between set-ups. For example, assuming a 10 mm streamwise thickness of the grid, the minimum width of the vertical bar is $w_{min} = 0.017$ given an aspect ratio $AR = 0.6$, which then determines the maximum possible c_n for each layer.

Since the number of bars c_n is restricted to be integers, the problem is solved by mixed integer nonlinear programming (MINLP), which is an active subject of research in optimization. There are many solvers available, and the results can be compared between different algorithms to give confidence. In principle, a homogeneous shear seems possible using this method where a linear profile of $U_{target,n}$ and a constant $u'_{target,n}$ are used as input to each one of these steps. This approach gives the framework of the grid design method, and the constraints in the problem can be improved and broadened to a wider range of turbulent shear flows with further studies.

3.4. *Reynolds shear stress*

In preparation of the model that we develop in § 3.5 to describe the streamwise evolution of the profiles $u'(y)$ from $x = 0.83$ m to larger values of x, we study in this section the streamwise development of the shear correlation coefficient $\rho \equiv -\overline{uv}/u'v'$ given in figure 12(*a*). It can be observed that, except for grid 1, all values decrease monotonically with streamwise distance. It is interesting to explore if there is a scaling relation that collapses these data. We first look at the dimensionless time scale $\tau^* \equiv (x/\overline{U_c})|S_n| = (x/\overline{U_c})|\overline{\partial U_n/\partial y}|$ (where $\overline{U_c}$ is the streamwise mean velocity averaged over the x along the centreline at $y = 0.46$ m) used in previous studies as this is an important parameter to describe the evolution of shear flows. The results are shown in figure 12(*b*), and $\overline{U_n}$ and $S_n \equiv \overline{\partial U_n/\partial y}$ are the averages of values measured at $x = 0.83$ m and $x = 4.13$ m. It is clear that the data do not collapse, especially for grid 2 and 3. If we use a modified local dimensionless time scale defined as $\tau \equiv [(x - x_{*,n}^{peak})/\overline{U_n}]|S_n|$, it can be seen that ρ is collapsed fairly well for $\tau \geqslant 0.8$. This definition of τ replaces $\overline{U_c}$ with $\overline{U_n}$, and includes the wake interaction length scale $x_{*,n}^{peak}$ as the virtual origin, since x_*^{peak} marks the starting location of decay that varies from layer to layer for each grid. This new definition of τ is equivalent to a translation of τ^* for regular grids, where x_*^{peak} is constant at all positions. The results can be compared between figure 12(*b*,*c*), where the profiles of ρ of grids 2 and 3 collapse much better with τ.

https://doi.org/10.1017/jfm.2018.387 Published online by Cambridge University Press

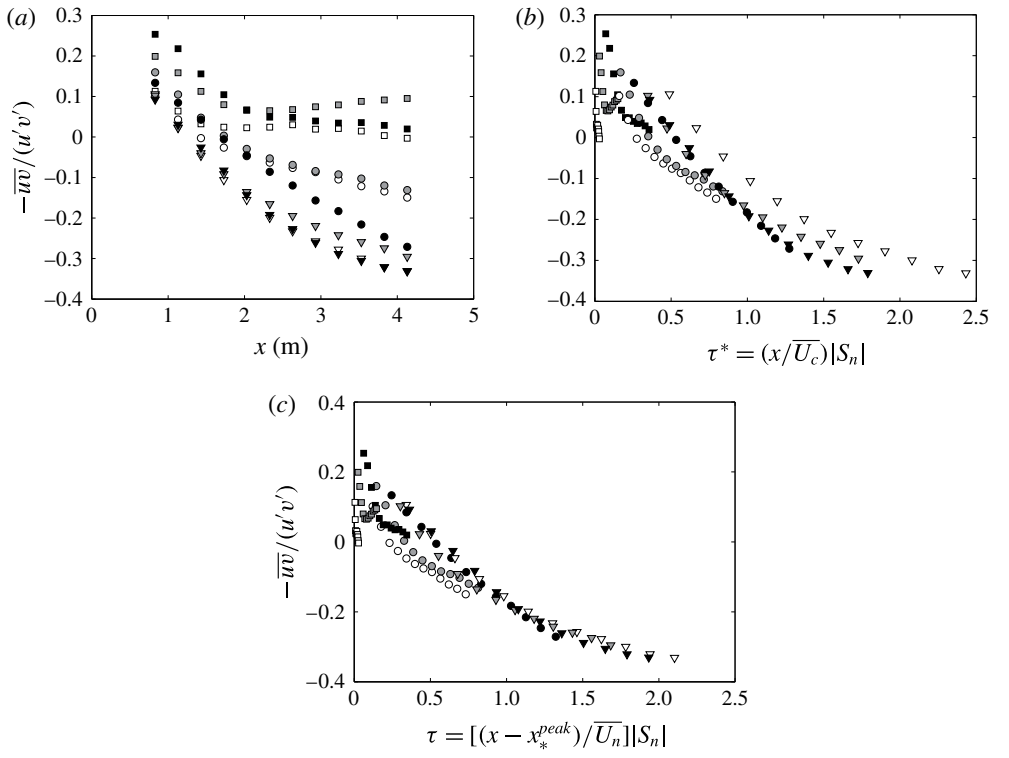


FIGURE 12. Streamwise development of $-\overline{uv}/u'v'$ for grid 1 (square), grid 2 (circle) and grid 3 (triangle) along the streamwise direction at $y = 0.25$ m (white), $y = 0.46$ m (grey) and $y = 0.66$ m (black) versus (*a*) streamwise location x, (*b*) local dimensionless time scale $\tau^* \equiv (x/\overline{U_c})|S_n|$, and (*c*) local dimensionless time scale $\tau \equiv [(x - x_{*,n}^{peak})/\overline{U_n}]|S_n|$ with virtual origin $x_{*,n}^{peak}$.

In several previous experiments (e.g. Rose 1966; Harris *et al.* 1977; Tavoularis & Corrsin 1981; Tavoularis & Karnik 1989; Nedić & Tavoularis 2016) it has been shown that the value of the shear correlation coefficient ρ increases downstream along the centreline and eventually reaches a magnitude of approximately 0.45–0.5. For the current results, it is interesting that the shear coefficient ρ changes sign for grids 2 and 3, but not for grid 1. Figure 12(*b*,*c*) suggest that the flow is greatly disrupted by the initial conditions that have an effect up to approximately $\tau = 0.8$, downstream of which the Reynolds shear stress starts to play a significant role. This makes sense by looking at grid 1 whose shear coefficient remains positive all the time and close to zero. The range of dimensionless time scale τ is not large enough to show the asymptote value of ρ (where $0.45 < |\rho| < 0.5$), although it seems that the change rate of ρ is decreasing with τ, which is consistent with previous literature.

The shear correlation coefficients $-\overline{uv}/u'v'$ along the y direction at $x = 0.83$ m and $x = 4.13$ m are shown in figure 13. The oscillatory behaviour at $x = 0.83$ m around $-\overline{uv}/u'v' = 0$ is most obvious as the probe moves behind the horizontal bars of the grid at every other y location. The large fluctuation of shear correlation coefficients with change of signs were also observed in e.g. Rose (1966) in a streamwise location close to the grid ($x/H = 1.33$). The positive-valued data points in figure 13(*a*) are from measurements taken at the centre of each layer (i.e. behind the vertical bars), which

https://doi.org/10.1017/jfm.2018.387 Published online by Cambridge University Press

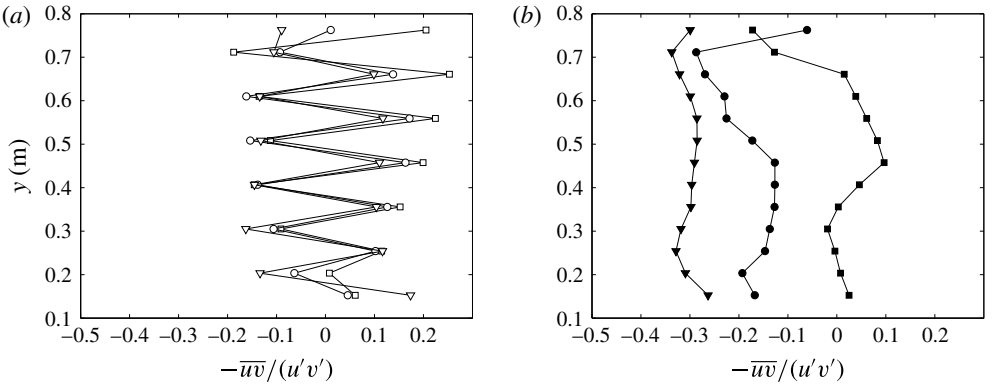


FIGURE 13. Vertical profiles of $-\overline{uv}/u'v'$ for grid 1 (square), grid 2 (circle) and grid 3 (triangle) at (a) $x = 0.83$ m (empty symbols) and (b) $x = 4.13$ m (filled symbols).

	$y = 0.26$ m			$y = 0.46$ m			$y = 0.66$ m		
	ρ_v	ρ_s	CI	ρ_v	ρ_s	CI	ρ_v	ρ_s	CI
Grid 1	0.1146	0.113	0.0016	0.1993	0.1989	0.0004	0.2531	0.2534	0.0003
Grid 2	0.102	0.1017	0.0003	0.1633	0.1594	0.0038	0.1378	0.1335	0.0042
Grid 3	0.1163	0.1058	0.0103	0.1102	0.1021	0.0079	0.0989	0.0923	0.0065

TABLE 3. Comparison of shear correlation coefficients measured from independent expriments at $x = 0.83$ m and different y locations. The 95 % confidence interval (CI) is calculated as $CI = 1.96\mathrm{cov}(\rho_v, \rho_s)/\sqrt{2}$, where ρ_v, ρ_s is the shear correlation coefficient measured from the vertical and streamwise profiles, respectively, and $\mathrm{cov}(\rho_v, \rho_s)$ is the covariance of ρ_v, ρ_s.

correspond to the data at $x = 0.83$ m given in figure 12(*a*). This also supports the assumption that direct effects of the grid dominate in the region of $\tau < 0.8$ as shown in figure 12. Table 3 gives the error of the shear correlation coefficients from two independent experiments to give confidence in the measurement, indicated by the 95 % confidence interval $CI = 1.96\mathrm{cov}(\rho_x, \rho_y)/\sqrt{2}$, where $\mathrm{cov}(\rho_s\rho_v)$ is the covariance of ρ_s, ρ_v measured from the streamwise and vertical profiles, respectively. In figure 13(*b*), it is observed that the magnitude of the shear coefficients increases from grid 1 to grid 3 (with increasing shear rate), and the variation of $-\overline{uv}/u'v'$ along the y direction is much reduced comparing to that measured at $x = 0.83$ m. This is consistent with the streamwise profiles discussed above, and previous observations made by Rose (1966), Garg & Warhaft (1998), Nedić & Tavoularis (2016).

3.5. *A simplified model for turbulent kinetic energy*

To look at the evolution of the y profiles of u' along the streamwise direction x, we have to consider the turbulence production by the mean shear rate, and we propose a simplified model to describe how $u'(x, y)$ evolves in the x direction downstream of our grids. To begin with, we neglect the pressure, transport and viscous diffusion terms in the turbulent kinetic energy equation. Harris *et al.* (1977) estimated the significance of the transport term by showing that the ratio $|(\partial\overline{u^3}/\partial x)/(U_c\partial\overline{u^2}/\partial x)|$ is smaller than

https://doi.org/10.1017/jfm.2018.387 Published online by Cambridge University Press

0.03 in their experiment, and concluded that the transport term can be omitted. In the current study, this ratio decreases rapidly with streamwise distance away from the grid, and the maximum values on the centreline (at $x = 0.83$ m) are 0.0105, 0.0102, 0.0113 for grids 1, 2, 3, respectively. We therefore assume that the transport is relatively small compared to the advection term, and that it can be neglected.

With these assumptions, we keep only the production and dissipation terms in the right-hand side of the kinetic energy equation following Harris *et al.* (1977) and Tavoularis & Corrsin (1981), i.e.

$$U\frac{\partial k}{\partial x} = P - \epsilon. \tag{3.6}$$

Then we write $P \cong -\overline{uv}S_n = \rho S_n u'v' = \rho^* S_n u'^2$, where $S_n \equiv \overline{\partial U_n/\partial y}$ is the local mean shear rate, and $\rho^*(x) = \rho(x)/\sqrt{2}$ because $v' = u'/\sqrt{2}$ as discussed in § 3.2. By assuming that the transverse r.m.s. fluctuating velocity w' equals v', i.e. $w' = v'$, the turbulent kinetic energy can then be written as $k = (1/2)(u'^2 + 2v'^2) = u'^2$. Finally we write the dissipation ϵ as $\epsilon = C_\epsilon(k^{3/2}/L) = C_\epsilon(u'^3/L)$, where $L = L_{uu,x}(x)$ is the longitudinal integral length scale.

Equation (3.6), for a given n or y (therefore omitted in the equations for simplicity), now becomes

$$U\frac{\partial u'^2}{\partial x} = \rho^*(x)Su'^2 - \frac{C_\epsilon(x)}{L(x)}u'^3. \tag{3.7}$$

To continue with a quantitative description of $u'(x, y)$, we write (3.7) at given n as

$$\frac{\mathrm{d}k}{\mathrm{d}x} + \xi(x)k = \zeta(x)k^m, \tag{3.8}$$

where $\xi(x) = -\rho^*(x)S/U$, $\zeta(x) = -C_\epsilon(x)/(UL(x))$ and $m = 3/2$.

The solution of (3.8) is given by

$$k = \left(\frac{-\frac{1}{2}\displaystyle\int_{x_p}^{x} \mathrm{e}^{-1/2\int_{x_p}^{x} -\rho^* S/U\,\mathrm{d}x} \left(\frac{-C_\epsilon}{UL}\right)\mathrm{d}x + C}{\mathrm{e}^{-1/2\int_{x_p}^{x} -\rho^* S/U\,\mathrm{d}x}} \right)^{-2}, \tag{3.9}$$

where we write $x_p \equiv x_*^{peak}$ for simplicity. To close (3.9), we need the expressions of $\rho^*(x)$, $L(x)$, $C_\epsilon(x)$ and the integration constant C. Since $\rho(\tau)$ collapses well in the way shown in figure 12(*c*), we fit $\rho^* = \rho/\sqrt{2}$ using a second-order polynomial (dashed lines) as shown in figure 14 to calculate $\rho^*(x)$ since x_*^{peak}, U_n and S_n in τ are known at given y. Here we fit the data with the centreline values of each grid (i.e. grey symbols), and the result captures the evolution of ρ^* quite well. This fitted function is then used to prescribe $\rho^*(x)$ given local constants x_*^{peak}, U_n and S_n. This fitting method inevitably carries larger error for grid 1 (see figure 14) due to the scatter of $\rho^*(x)$ at $\tau \approx 0$. But the mean shear rate produced by grid 1 is approximately 0, and the power $(-0.5S/U\int_{x_p}^{x} -\rho^*\,\mathrm{d}x)$ in the exponential is effectively 0 too, which makes the error for grid 1 insignificant in (3.9).

https://doi.org/10.1017/jfm.2018.387 Published online by Cambridge University Press

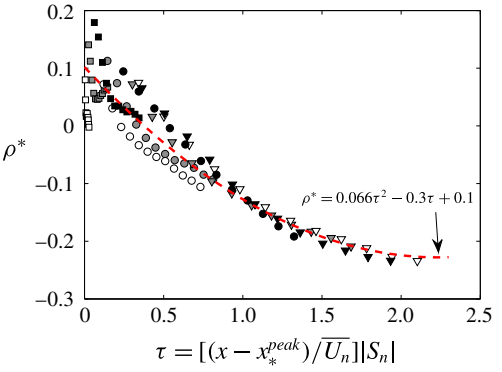


FIGURE 14. (Colour online) Streamwise profiles of ρ^* for grid 1 (square), grid 2 (circle) and grid 3 (triangle) at $y = 0.25$ m (white), $y = 0.46$ m (grey) and $y = 0.66$ m (black) with second-order polynomial fit (dashed lines).

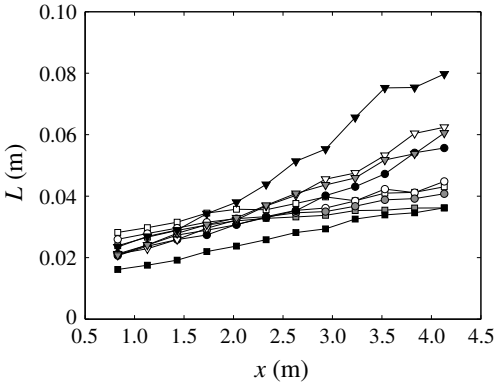


FIGURE 15. Longitudinal integral length scale L profiles for grid 1 (square), grid 2 (circle) and grid 3 (triangle) at $y = 0.25$ m (white), $y = 0.46$ m (grey) and $y = 0.66$ m (black) versus the streamwise location x.

3.5.1. *Integral length scale*

Now we look at the development of the longitudinal integral length scale L as a function of the streamwise location x for all grids, see figure 15. The length scales are calculated using the corrected spectra as discussed in § 2.3. It is obvious that L increases with the streamwise location monotonically. The value of L for a given grid at different y locations seems to grow linearly at a rate which is practically similar at different y locations. This also implies that L increases approximately linearly against the local dimensionless time scale τ as well, which is consistent with Champagne *et al.* (1970) and Harris *et al.* (1977).

By looking at the profiles along y in figure 16, it seems that L remains roughly constant at $x = 0.83$ m. At $x = 4.13$ m, the value of L increases from grid 1 (square) to grid 3 (triangle). This makes sense if $L \propto \tau$, as τ increases with the mean shear rate S at given x and U.

From figures 15 and 16, we notice that the values of L at $y = 0.66$ m are smaller for grid 1 and larger for grid 3, yet the values calculated at this location from the two independent measurements are the same (as shown in figures 15 and 16), which rules

https://doi.org/10.1017/jfm.2018.387 Published online by Cambridge University Press

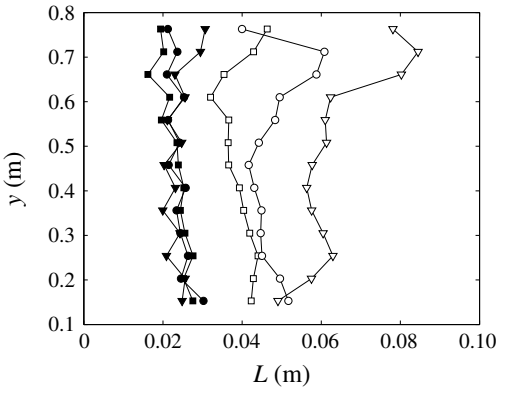


FIGURE 16. Longitudinal integral length scale L profiles for grid 1 (square), grid 2 (circle) and grid 3 (triangle) along the y direction at $x = 0.83$ m (filled symbols) and $x = 4.13$ m (empty symbols).

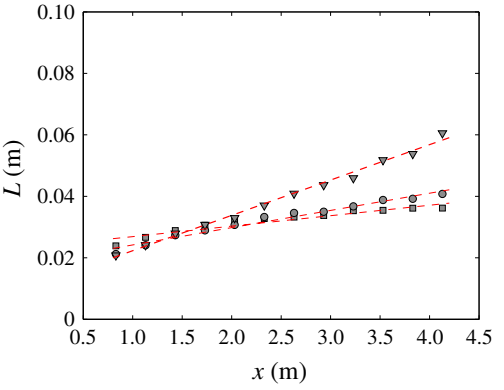


FIGURE 17. (Colour online) Profiles of longitudinal integral length scale L for grid 1 (square), grid 2 (circle) and grid 3 (triangle) along the centreline with linear fitted results (dashed lines).

out the possibility of measurement/calculation error. The reason for this larger value is not completely clear, but might have to do with the different inlet grid conditions and the related different mean shear rates.

For the purpose of the current discussion, we ignore this outlier, and assume that the rate of increase of L for a given grid is independent of y. We therefore estimate the streamwise evolution of L based on its centreline profile only. The fitted results are given in figure 17, where all three profiles show a linear increase with streamwise distance x away from the grid. This is also consistent with previous works such as Champagne *et al.* (1970) and Harris *et al.* (1977). We write $L(x) = px + q$, where p, q are fitting coefficients. The fitted constants are $p = 0.0034$, 0.0056, 0.012 and $q = 0.024$, 0.019, 0.011 for grid 1, 2, 3, respectively.

3.5.2. *Dissipation coefficient* C_ϵ

The behaviour of C_ϵ in turbulent shear flow with uniform mean shear rate has been studied by Nedić & Tavoularis (2016), where they showed different stages of

https://doi.org/10.1017/jfm.2018.387 Published online by Cambridge University Press

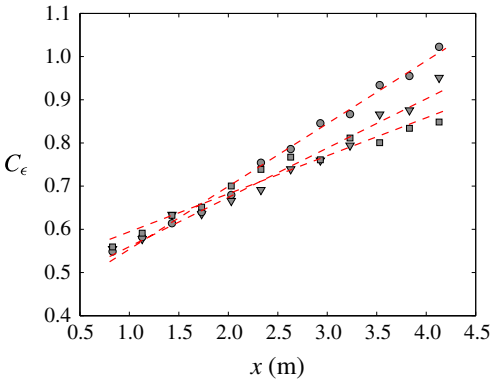


FIGURE 18. (Colour online) Profiles of $C_\epsilon = \epsilon L/u'^3$ for grid 1 (square), grid 2 (circle) and grid 3 (triangle) along the centreline with linear fitted results (dashed lines).

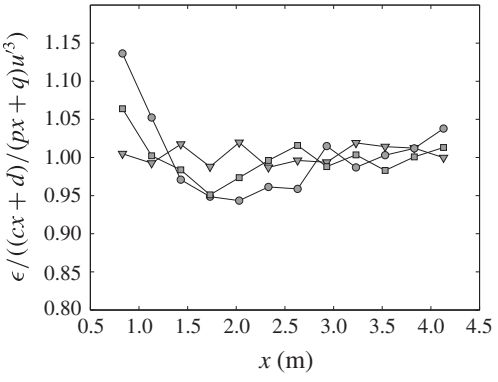


FIGURE 19. Ratio of ϵ and modelled term $(cx+d)/(px+q)u'^3$ grid 1 (square), 2 (circle) and 3 (triangle), respectively, along the centreline.

development with respect to τ. In figure 18, we show the streamwise development of $C_\epsilon = \epsilon L/u'^3$ along the centreline for all three grids. It can be observed that all three profiles increase linearly as $C_\epsilon = cx + d$, where the coefficients c, d are fitted in a least square sense. The fitted constants are $c = 0.088$, 0.15, 0.11 and $d = 0.51$, 0.41, 0.45 for grids 1, 2, 3 respectively. This linear increase of C_ϵ with x is in agreement with Nedić & Tavoularis (2016) in their initial region.

To check the quality of our linear fits of $C_\epsilon(x)$ and $L(x)$, we plot the ratio $\epsilon/(C_\epsilon u'^3/L)$ as $\epsilon/((cx+d)u'^3/(px+q))$ in figure 19. It is observed that this ratio is within $\pm 5\,\%$ of unity for all three grids, with the exception of the first point.

3.5.3. *Predicting streamwise evolution*

With the fitted functions of $\rho^*(x)$, $L(x)$ and $C_\epsilon(x)$, we can now solve (3.9) for the turbulence intensity profile $u'(y)$ at given streamwise location $x = 0.83$ m. Figure 20 shows the result of both the measured turbulence intensity profiles $u'(x, y)/U_\infty$, and profiles calculated using (3.9), where $k = u'^2$, $S = \overline{S_n}$ and $U = \overline{U_n}$. The vertical profile measured at $x = 0.83$ m (where the turbulence intensity is highest, i.e. the first profile on the right) is used as initial values to calculate the constant $C = C(n)$ so the collapse

https://doi.org/10.1017/jfm.2018.387 Published online by Cambridge University Press

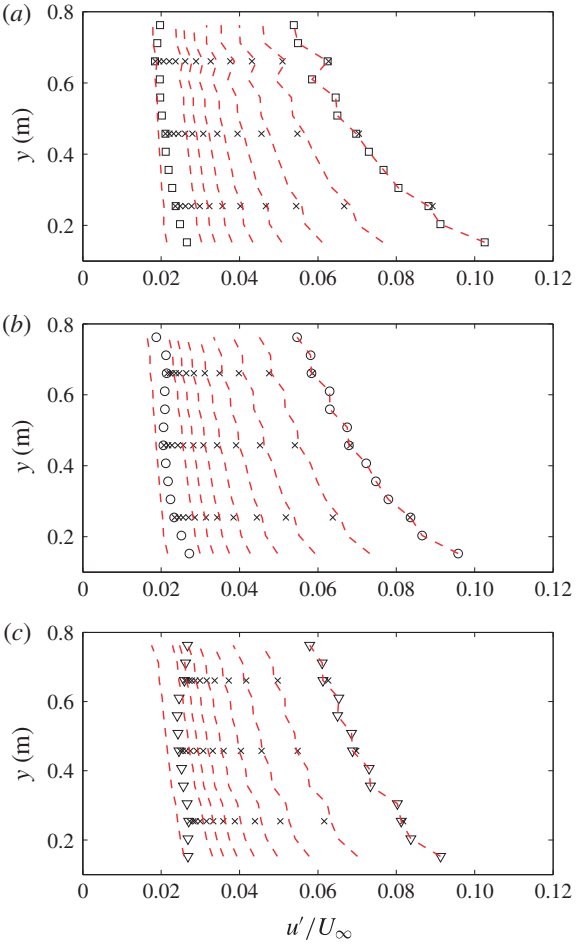


FIGURE 20. (Colour online) Turbulence intensity profiles u'/U_∞ for (*a*) grid 1 (square), (*b*) grid 2 (circle) and (*c*) grid 3 (triangle). Empty symbols are vertical profiles measured at $x = 0.83$ m and $x = 4.13$ m. Cross symbols are streamwise profiles measured at given y location. Dashed red lines are predictions calculated using the vertical profile and centreline profile.

of this profile is perfect. The fitted values of C at selected y locations are given in table 4. The measured streamwise profiles are plotted at their corresponding height y, and are used to check the results calculated at different x locations. Each profile is separated by $\Delta x = 0.3$ m. Small discrepancies between the measured and calculated values are observed, which might come from the neglected terms in (3.7) and the fitting of the centreline profiles. Nevertheless, the results are in appreciable agreement up to $x = 2.33$ m, which is equivalent to $x/H = 2.6$, where H is the height of the grid (i.e. height of the tunnel). For grid 3, it is noticed that the discrepancy between measured turbulence intensity and modelled result at $x = 4.13$ m (first profile on the left) is the largest, especially at higher y locations. This can be partially explained by the discussion in § 3.5.1 about L increasing faster for grid 3 around $y = 0.7$ m. Also, streamwise turbulence intensity developments of shear flows such that u'/U_∞ stops decaying (or starts increasing) at larger τ have been reported by e.g. Rohr *et al.*

https://doi.org/10.1017/jfm.2018.387 Published online by Cambridge University Press

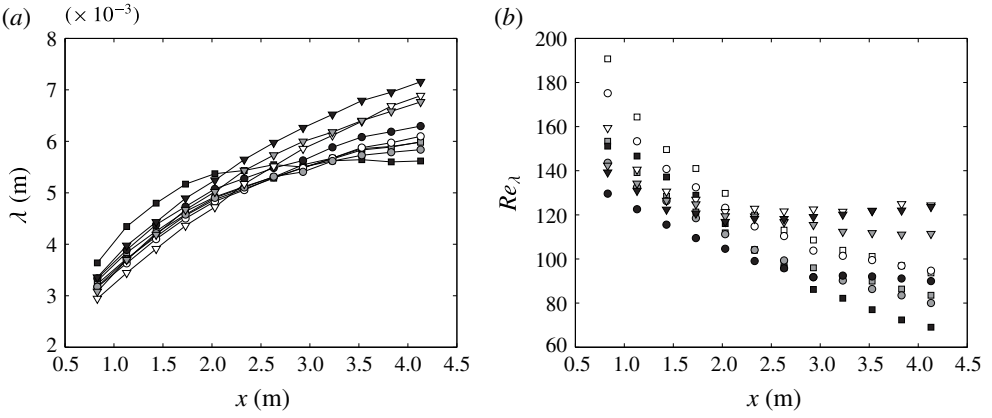


FIGURE 21. Streamwise profiles of (*a*) Taylor microscale λ, and (*b*) local Reynolds number Re_λ for grid 1 (square), grid 2 (circle) and grid 3 (triangle) at $y = 0.25$ m (white), $y = 0.46$ m (grey) and $y = 0.66$ m (black).

$y(m)$	Grid 1	Grid 2	Grid 3
0.66	0.82	0.82	0.29
0.46	0.67	0.67	0.31
0.25	0.43	0.50	0.33

TABLE 4. Fitted constant C in (3.9) at selected y locations for all grids.

(1988), Tavoularis & Karnik (1989). In such case, flow characteristics such as C_ϵ, ρ and L all evolve in different ways compared to their initial development as discussed by Nedić & Tavoularis (2016). A more comprehensive model of the problem will require measurements at further stages of the turbulent kinetic energy evolution in terms of τ. Nevertheless, the current method provides a practical solution for the near-region (i.e. up to $x/H = 2.6$, where H is the height of the grid) turbulent kinetic energy development of our multiscale grid-generated shear flow, and can be of practical use in the study of turbulent shear flows and engineering applications.

3.6. *Taylor microscales*

In this section we report Taylor microscale values calculated from $\lambda = u'/(\overline{(\partial u/\partial x)^2})^{1/2}$. Figure 21(*a*) gives the streamwise development of λ versus x. It can be observed that λ increases with x in all cases. This agrees well with several previous experiments such as Rose (1966), Champagne *et al.* (1970). Tavoularis & Karnik (1989) also showed a region $\tau^* > 16$, where λ remains constant against τ. This is not observed here due to the small mean shear rates. We also report the local Reynolds number $Re_\lambda = u'\lambda/\nu$ along the x direction, where ν is the kinematic viscosity. Their values decrease monotonically for grid 1 and grid 2. For grid 3, a mild increase after $x = 2.5$ m is observed, which corresponds to its higher turbulence intensity u' (see figure 8*a*), and the larger value of λ (see figure 21*a*). This is in agreement with the observation of Nedić & Tavoularis (2016) where they showed an increase of Re_λ after $\tau^* > 4.5$.

https://doi.org/10.1017/jfm.2018.387 Published online by Cambridge University Press

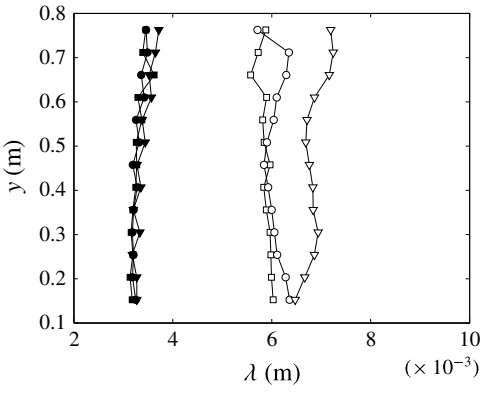


FIGURE 22. Taylor microscale λ profiles for grid 1 (square), grid 2 (circle) and grid 3 (triangle) along the y direction at $x = 0.83$ m (filled symbols) and $x = 4.13$ m (empty symbols).

	Grid 1			Grid 2			Grid 3		
x (m s^{-1})	0.83	2.33	4.13	0.83	2.33	4.13	0.83	2.33	4.13
x/H	0.91	2.55	4.52	0.91	2.55	4.52	0.91	2.55	4.52
U/U_∞	1.006	1.012	1.011	1.004	1.004	0.996	0.999	0.987	0.979
u'/U_∞	0.07	0.031	0.021	0.068	0.031	0.021	0.070	0.033	0.025
Re_λ	153.4	119.3	111.4	143.6	104.1	80.06	142.3	119.3	111.4
$-\overline{uv}/u'v'$	0.199	0.065	0.095	0.159	−0.053	−0.131	0.102	−0.166	−0.296
$\overline{(\partial v/\partial x)^2}/\overline{(\partial u/\partial x)^2}$	0.941	1.071	1.091	0.938	1.074	1.091	0.963	1.099	1.129
u'/v'	1.41	1.37	1.39	1.40	1.37	1.36	1.44	1.42	1.46
$L_{uu,x}/L_{vv,x}$	2.12	1.84	1.58	1.98	1.89	1.67	1.96	1.94	2.12

TABLE 5. Summary of centreline turbulence characteristics at different streamwise locations for different grids at $Re_D = 8500$ based on the width of the vertical grid bar.

Along the shear direction y, Rose (1966) reported decreasing values of λ with increasing local mean velocity, whereas Champagne *et al.* (1970) showed roughly constant values of λ along the shear direction. The shear rates of the two cases are similar, i.e. $\partial U/\partial y = 13.6$ s^{-1} and 12.9 s^{-1}, respectively, so it seems the shear rate is not the reason for this difference. Note however, Rose (1966) used wire gauze with different spacings along the shear direction as a generator, while Champagne *et al.* (1970) used parallel plates with equal spacing but different local blockage ratios to generate the shear flow. There are no more data available for a more comprehensive conclusion, but the current study is similar to that of Champagne *et al.* (1970), in that the layer height is constant with varying local blockage ratios, and therefore it might be expected to have a roughly constant y-profile of λ. The results of the Taylor microscale λ along the y direction at $x = 0.83$ m and $x = 4.13$ m are given in figure 22, and it indeed seems roughly constant.

3.7. *Flow isotropy*

Having shown the streamwise development of turbulence intensities and length scales, we now examine the isotropy of the flow. Some of the results are given in table 5

https://doi.org/10.1017/jfm.2018.387 Published online by Cambridge University Press

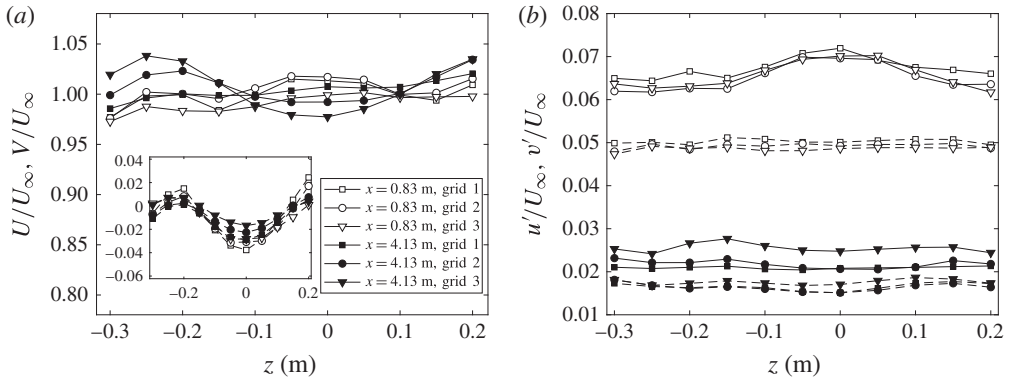


FIGURE 23. Transverse profiles of (*a*) mean velocity U/U_∞ (symbols with solid line) and V/U_∞ (inset, symbols with dashed line); (*b*) turbulence intensity u'/U_∞ (symbols with solid line) and v'/U_∞ (symbols with dashed line) across the centre of the grid where $y/H = 0.5$.

at different x locations along the centreline at $y = 0.46$ m. The small scale isotropy indicator $\overline{(\partial v/\partial x)^2}/\overline{(\partial u/\partial x)^2}$ seems to suggest that the flow is anisotropic as the ratio is much smaller than the isotropic value of 2, even though they are increasing along the x direction. These results are in agreement with previous observations made by Shen & Warhaft (2000) and Schumacher (2001).

It is interesting that the results close to the grid suggest large scale isotropy of the flow such that $L_{uu,x}/L_{vv,x} = 2$, but $u'/v' \approx 1.4$ on the other hand. These values are maintained best by grid 3 if we compare the values at different streamwise locations in table 5. Intuitively, the shearing stress is expected to strain the large scale structure along the mean shear direction and impose anisotropy to the flow, which seems to counter our observation that $L_{uu,x}/L_{vv,x} = 2$. Similar observations have been reported before, for example Rose (1966) showed $L_{uu,x}/L_{uu,y} = 2$ and $u'/v' \approx 1.5$ in a turbulent shear flow generated by a parallel wire grid, and Tavoularis & Corrsin (1981) reported $L_{uu,x}/L_{vv,x} = 4.34$ with $u'/v' \approx 1.4$ in a parallel plate-generated turbulent shear flow. These observations seem to suggest that the ratio of $L_{uu,x}/L_{vv,x}$ and u'/v' reflect different aspects of anisotropy of the flow, and do not need to take their isotropic values concordantly.

3.8. *Transverse homogeneity*

The transverse homogeneity of the shear flow is discussed in this section. The mean velocity and turbulence intensity profiles are given in figure 23(*a*,*b*), respectively, measured at $x = 0.83$ m (or $x/H = 0.91$, open symbols) and $x = 4.13$ m (or $x/H = 4.52$, filled symbols) across the centre of the grid at $y = 0.46$ m or $y/H = 0.5$. From figure 23(*a*), it is observed that the transverse profiles of the streamwise mean velocity are more homogeneous closer to the grid, whereas the vertical mean velocity is more homogeneous further downstream (filled symbol with dashed line in the inset). A sinusoidal variation seems to be present for the streamwise mean velocity profiles measured at $x = 4.13$ m, and the profiles seem to be symmetric about the centre plane $z = 0$ m, although the variations are all within $8\,\%U_\infty$. For the mean velocity profiles of V/U_∞, the sinusoidal variation is also observed symmetric about the centre plane, and the amplitude is smaller (within $5\,\%\ U_\infty$). The symmetry is due to the alignment of the vertical bars at $z = 0$ m, and might be reduced by arranging the vertical bars in a staggering pattern.

https://doi.org/10.1017/jfm.2018.387 Published online by Cambridge University Press

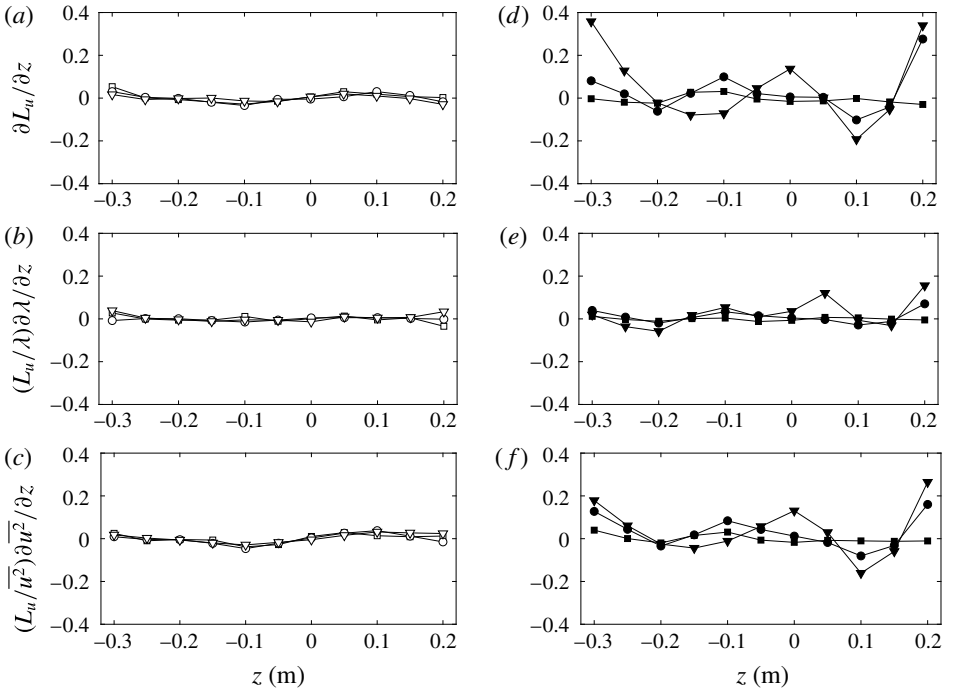


FIGURE 24. Homogeneity of the transverse profiles for grid 1 (square), grid 2 (circle) and grid 3 (triangle) at $x = 0.83$ m (or $x/H = 0.91$, open symbols) and $x = 4.13$ m (or $x/H = 4.52$, filled symbols) across the centre of the grid at $y/H = 0.5$.

This symmetry is also observed in the transverse profiles of streamwise turbulence intensity u'/U_∞ at $x = 0.83$ m, as shown in figure 23(*b*) with open symbol and solid line. Nevertheless, the variation of the turbulence intensity is within 1 % U_∞. The transverse profiles of v'/U_∞ seems to be more homogeneous in all cases. We therefore further quantify the homogeneity of the streamwise properties in the transverse direction, referring to the criteria proposed by Corrsin (1963), namely

$$\partial L_u/\partial z \ll 1, \tag{3.10a}$$

$$(L_u/\lambda)\partial\lambda/\partial z \ll 1, \tag{3.10b}$$

$$(L_u/\overline{u^2})\partial\overline{u^2}/\partial z \ll 1. \tag{3.10c}$$

The results are given in figure 24 for measurements taken at $x = 0.83$ m (open symbols), and $x = 4.13$ m (filled symbols).

The values of the homogeneity criteria, as shown in figure 24, are all smaller at the streamwise location closer to the grid. The values calculated at $x = 0.83$ m are all within ± 0.05 as seen in figure 24(*a–c*). These figures suggest that the transverse homogeneity of the shear flow is better at $x = 0.83$ m, or $x/H = 0.91$, which is a nice trait as the turbulence intensity level is higher in this region.

4. Conclusions

In this paper we proposed a new class of inhomogeneous multiscale grids, and examined the turbulent shear flows generated by these grids using hot-wire

https://doi.org/10.1017/jfm.2018.387 Published online by Cambridge University Press

anemometry. There are three major conclusions from the shear flows generated by these grids:

(i) Generation of a desired mean velocity profile is possible by optimizing the blockage ratio profile σ_n, while maintaining a constant C_D profile of the vertical bars. The drag coefficient of the vertical bars was found to affect the mean velocity profiles significantly, and it is therefore important to maintain a constant C_D. The mean velocity model after Taylor *et al.* (1949) and McCarthy (1964) based on the local blockage ratio σ_n was shown to agree with our measurements, with mean shear rates of 0.29 s^{-1}, 2.97 s^{-1} and 4.99 s^{-1} for grids 1, 2 and 3, respectively. The maximum possible mean shear rate generated by these grids depends on the size of the test facility as the maximum local blockage ratio is always constrained by $\sigma_n < 0.4$.

(ii) High turbulence intensities can be generated simultaneously with the desired mean velocity profile. The maximum turbulence intensities generated by the present grids are of the order of 10 % U_∞, which is much larger than those generated by previously reported passive shear generators, and it seems possible to prescribe the shape of the turbulence intensity profile. From the scalings proposed by Gomes-Fernandes *et al.* (2012), and by considering the non-uniform convection velocity, it was shown that at a streamwise location $x = x_m$ such that $x_m/x_*^{peak} > 1$ ($x_m/H = 0.9$ for the current cases), the y-profiles of turbulence intensity $u'(y)$ scale as $(u'/U_n)^2\beta^2(C_D w_n/x_{*,n}^{peak})^{-1} \sim (x_m/x_{*,n}^{peak})^b$, where $\beta = 2.88$ is a constant, U_n is the local (in y or equivalently n) mean velocity and b is a power law constant. Based on this scaling relation, it seems possible to optimize the grid geometry to produce a desired shape of turbulence intensity profile. From the mean velocity model and the scaling of turbulence intensity, a general approach to the design of multiscale inhomogeneous grids is proposed and briefly discussed in § 3.3. The methodology can be improved by adding more constraints to the optimization problem, as new results of such experiments emerge.

(iii) For a given grid, the generated turbulence field can be described using one centreline measurement along the streamwise direction and one vertical profile at $x/x_*^{peak} > 1$. For the current study, the proposed model successfully predicts the y-profiles of u' at different x locations up to $x/H \approx 2.5$ for all cases as shown in figure 20. The evolution of various flow characteristics included in the model was also studied and compared with previous literature.

There are some other interesting observations of the shear flows generated by these multiscale grids such as the spectra, as briefly discussed in the Appendix. In terms of future work, the potential of the grid design method should be explored further to establish the range of turbulent shear flows that can be produced. The special case of homogeneous turbulent shear flows could be attempted with our grid design method because of the long standing fundamental interest in such flows. Due to the small mean shear rate, the dimensionless time scale ranges from $\tau = 0$ to 2.3. So it is also interesting to extend the range of measurement to larger dimensionless time scale τ, where the development of various turbulence characteristics and length scales could be further examined. This can be achieved by either extending the measurement distance or increasing the mean shear rate. Measurements with multiple hot-wires will also help to understand the neglected terms in the turbulent kinetic energy model. Such studies, if successful, would provide another option to design a shear flow with desired mean velocity and turbulence intensity profiles, which will benefit both fundamental studies and a wide range of practical applications.

https://doi.org/10.1017/jfm.2018.387 Published online by Cambridge University Press

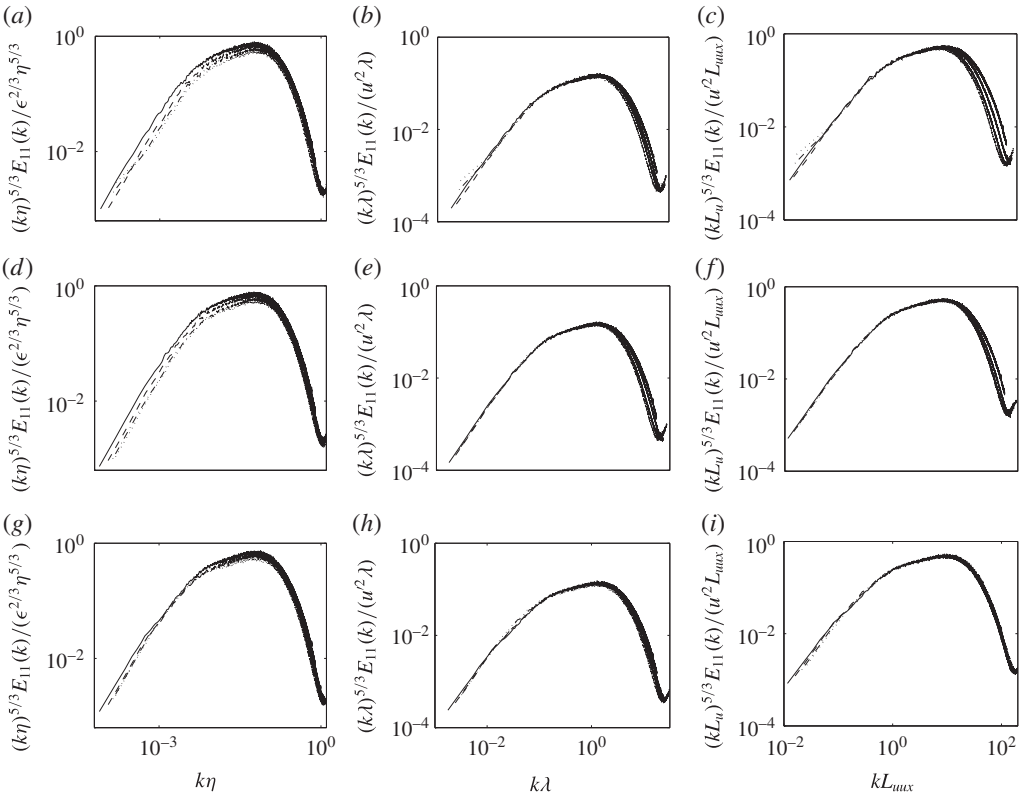


FIGURE 25. Turbulence spectra $E_{11}(k)$ at four x locations (0.83 m, 2.13 m, 2.93 m and 3.83 m) along the centreline at height $y = 0.46$ m for grid 1 (*a–c*), grid 2 (*d–f*) and grid 3 (*g–i*), compensated for η, λ, and L, respectively.

Acknowledgements

The authors gratefully acknowledge support from Marie Curie FP7 through the MULTISOLVE project, grant number 317269. J.C.V. also acknowledges support from ERC Advance Grant 320560.

Appendix. Spectra

The spectra for all three grids are presented here at four streamwise locations for reference, namely $x = 1.13$ m, 2.03 m, 2.93 m, 3.83 m. The Reynolds number is in the range of $70 < Re_\lambda < 190$. First of all, considering grid turbulence, the one-dimensional spectra are expected to collapse at corresponding range when normalized with $L_{uu,x}$, λ and η, respectively. Figure 25 shows the spectra measured at different x locations along the centreline at height $y = 0.46$ m. It shows that the spectra collapse well in the small wavenumber range when normalized with L, and in the large wave number range when normalized with η. This is consistent with those conclusions for homogeneous isotropic turbulence.

It is also observed from figure 25 such that for all scaling methods, the quality of collapse improves from grid 1 to grid 3, and it is interesting that for grid 3, the integral length scale L_{uux} seems to collapse the spectra at all wavenumbers. The reason for this is not exactly clear.

https://doi.org/10.1017/jfm.2018.387 Published online by Cambridge University Press

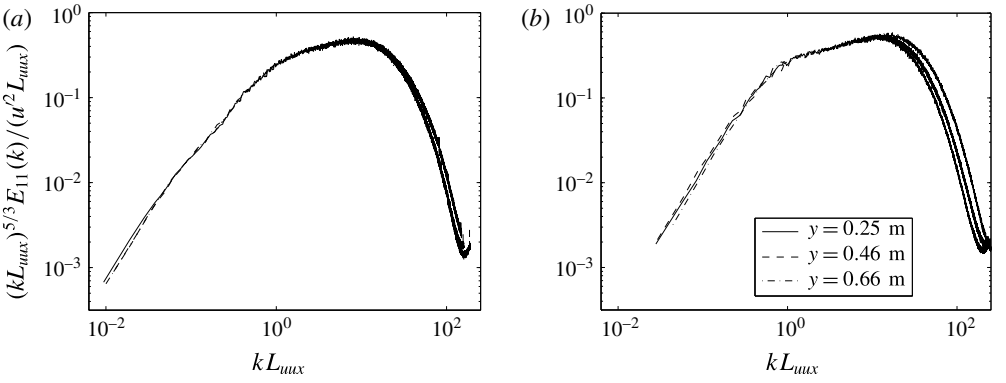


FIGURE 26. Turbulence spectra $E_{11}(k)$ at several y locations compensated for L at (*a*) $x = 0.83$ m, and (*b*) $x = 4.13$ m.

When the spectra of grid 3 at different y locations are plotted together, as shown in figure 26, the collapse is not observed even when compensated using the longitudinal integral length scale $L_{uu,x}$, and the difference seems to increase with streamwise distance. These observations suggests the dependency of $E(k)$ on the initial conditions of the grid, but this dependency cannot be quantified at the moment.

REFERENCES

BAI, K., MENEVEAU, C. & KATZ, J. 2012 Near-wake turbulent flow structure and mixing length downstream of a fractal tree. *Boundary-Layer Meteorology* **143** (2), 285–308.

BEARMAN, P. W. & TRUEMAN, D. M. 1972 Investigation of flow around rectangular cylinders. *Aeronaut. Q.* **23** (AUG), 229–237.

BOTTIN, S., DAUCHOT, O., DAVIAUD, F. & MANNEVILLE, P. 1998 Experimental evidence of streamwise vortices as finite amplitude solutions in transitional plane couette flow. *Phys. Fluids* **10** (10), 2597–2607.

CARDESA, J. I., NICKELS, T. B. & DAWSON, J. R. 2012 2D PIV measurements in the near field of grid turbulence using stitched fields from multiple cameras. *Exp. Fluids* **52** (6), 1611–1627.

CEKLI, H. & VAN DE WATER, W. 2010 Tailoring turbulence with an active grid. *Exp. Fluids* **49** (2), 409–416.

CHAMPAGNE, F. H., HARRIS, V. G. & CORRSIN, S. 1970 Experiments on nearly homogeneous turbulent shear flow. *J. Fluid Mech.* **41** (01), 81–139.

COLES, D. 1965 Transition in circular couette flow. *J. Fluid Mech.* **21** (3), 385–425.

COMTE-BELLOT, G. & CORRSIN, S. 1966 The use of a contraction to improve the isotropy of grid-generated turbulence. *J. Fluid Mech.* **25** (04), 657–682.

COMTE-BELLOT, G. & CORRSIN, S. 1971 Simple eulerian time correlation of full- and narrow-band velocity signals in grid-generated, isotropic turbulence. *J. Fluid Mech.* **48** (02), 273–337.

CORNELL, W. G. 1958 Losses in flow normal to plane screens. *Trans. ASME* **80** (4), 791–799.

CORRSIN, S. 1963 Turbulence: experimental methods. *Handbuch der Physik* **3**, 524–590.

DUNN, W. & TAVOULARIS, S. 2007 The use of curved screens for generating uniform shear at low Reynolds numbers. *Exp. Fluids* **42** (2), 281–290.

ELDER, J. W. 1959 Steady flow through non-uniform gauzes of arbitrary shape. *J. Fluid Mech.* **5** (03), 355–368.

GAD-EL-HAK, M. & CORRSIN, S. 1974 Measurements of the nearly isotropic turbulence behind a uniform jet grid. *J. Fluid Mech.* **62** (01), 115–143.

https://doi.org/10.1017/jfm.2018.387 Published online by Cambridge University Press

GARG, S. & WARHAFT, Z. 1998 On the small scale structure of simple shear flow. *Phys. Fluids* **10** (3), 662–673.

GOMES-FERNANDES, R., GANAPATHISUBRAMANI, B. & VASSILICOS, J. C. 2012 Particle image velocimetry study of fractal-generated turbulence. *J. Fluid Mech.* **711**, 306–336.

HARRIS, V. G., GRAHAM, J. A. H. & CORRSIN, S. 1977 Further experiments in nearly homogeneous turbulent shear flow. *J. Fluid Mech.* **81** (04), 657–687.

HEARST, R. J. & GANAPATHISUBRAMANI, B. 2017 Tailoring incoming shear and turbulence profiles for lab-scale wind turbines. *Wind Energy* **20** (12), 2021–2035.

HEARST, R. J. & LAVOIE, P. 2014 Decay of turbulence generated by a square-fractal-element grid. *J. Fluid Mech.* **741**, 567–584.

HURST, D. & VASSILICOS, J. C. 2007 Scalings and decay of fractal-generated turbulence. *Phys. Fluids* **19** (3), 035103.

ISAZA, J. C., SALAZAR, R. & WARHAFT, Z. 2014 On grid-generated turbulence in the near- and far field regions. *J. Fluid Mech.* **753**, 402–426.

KARNIK, U. & TAVOULARIS, S. 1987 Generation and manipulation of uniform shear with the use of screens. *Exp. Fluids* **5** (4), 247–254.

KNEBEL, P., KITTEL, A. & PEINKE, J. 2011 Atmospheric wind field conditions generated by active grids. *Exp. Fluids* **51** (2), 471–481.

LAWS, E. M. & LIVESEY, J. L. 1978 Flow through screens. *Annu. Rev. Fluid Mech.* **10** (1), 247–266.

LAWSON, T. V. 1968 Methods of producing velocity profiles in wind tunnels. *Atmos. Environ.* **2** (1), 73–76.

LIVESEY, J. L. & LAWS, E. M. 1973*a* Flow through non-uniform gauze screens. *J. Fluid Mech.* **59** (04), 737–743.

LIVESEY, J. L. & LAWS, E. M. 1973*b* Simulation of velocity profiles by shaped gauze screens. *AIAA J.* **11** (2), 184–188.

MAKITA, H. 1991 Realization of a large-scale turbulence field in a small wind tunnel. *Fluid Dyn. Res.* **8** (1–4), 53–64.

MAZELLIER, N. & VASSILICOS, J. C. 2010 Turbulence without Richardson–Kolmogorov cascade. *Phys. Fluids* **22** (7), 075101,1–25.

MCCARTHY, J. H. 1964 Steady flow past non-uniform wire grids. *J. Fluid Mech.* **19** (04), 491–512.

MOHAMED, M. S. & LARUE, J. C. 1990 The decay power law in grid-generated turbulence. *J. Fluid Mech.* **219**, 195–214.

MULHEARN, P. J. & LUXTON, R. E. 1975 The development of turbulence structure in a uniform shear flow. *J. Fluid Mech.* **68** (03), 577–590.

MYDLARSKI, L. & WARHAFT, Z. 1996 On the onset of high-Reynolds-number grid-generated wind tunnel turbulence. *J. Fluid Mech.* **320**, 331–368.

NEDIĆ, J. & TAVOULARIS, S. 2016 Energy dissipation scaling in uniformly sheared turbulence. *Phys. Rev.* E **93** (3), 033115.

O'NEILL, P. L., NICOLAIDES, D., HONNERY, D. & SORIA, J. 2004 Autocorrelation functions and the determination of integral length with reference to experimental and numerical data. In *15th Australasian Fluid Mechanics Conference*. The University of Sydney.

OWEN, P. R. & ZIENKIEWICZ, H. K. 1957 The production of uniform shear flow in a wind tunnel. *J. Fluid Mech.* **2** (06), 521–531.

RICHARDS, H. K. & MORTON, J. B. 1976 Experimental investigation of turbulent shear flow with quadratic mean-velocity profiles. *J. Fluid Mech.* **73** (01), 165–188.

ROACH, P. E. 1987 The generation of nearly isotropic turbulence by means of grids. *Int. J. Heat Fluid Fl.* **8** (2), 82–92.

ROHR, J. J., ITSWEIRE, E. C., HELLAND, K. N. & VAN ATTA, C. W. 1988 An investigation of the growth of turbulence in a uniform-mean-shear flow. *J. Fluid Mech.* **187**, 1–33.

ROSE, W. G. 1966 Results of an attempt to generate a homogeneous turbulent shear flow. *J. Fluid Mech.* **25** (01), 97–120.

ROSE, W. G. 1970 Interaction of grid turbulence with a uniform mean shear. *J. Fluid Mech.* **44** (04), 767–779.

https://doi.org/10.1017/jfm.2018.387 Published online by Cambridge University Press

SCHUMACHER, J. R. G. 2001 Derivative moments in stationary homogeneous shear turbulence. *J. Fluid Mech.* **441**, 109–118.

SEOUD, R. E. & VASSILICOS, J. C. 2007 Dissipation and decay of fractal-generated turbulence. *Phys. Fluids* **19** (10), 105108.

SHEN, X. & WARHAFT, Z. 2000 The anisotropy of the small scale structure in high Reynolds number ($Re \sim 1000$) turbulent shear flow. *Phys. Fluids* **12** (11), 2976–2989.

DE SOUZA, F. A., NGUYEN, V. D. & TAVOULARIS, S. 1995 The structure of highly sheared turbulence. *J. Fluid Mech.* **303**, 155–167.

TAVOULARIS, S. & CORRSIN, S. 1981 Experiments in nearly homogenous turbulent shear flow with a uniform mean temperature gradient. Part 1. *J. Fluid Mech.* **104**, 311–347.

TAVOULARIS, S. & KARNIK, U. 1989 Further experiments on the evolution of turbulent stresses and scales in uniformly sheared turbulence. *J. Fluid Mech.* **204**, 457–478.

TAYLOR, G. I., BATCHELOR, G. K., DRYDEN, H. L. & SCHUBAUER, G. B. 1949 The effect of wire gauze on small disturbances in a uniform stream. *Q. J. Mech. Appl. Math.* **2** (1), 1–29.

TENNEKES, H. & LUMLEY, J. L. 1972 *A First Course in Turbulence*. MIT Press.

THORMANN, A. & MENEVEAU, C. 2015 Decaying turbulence in the presence of a shearless uniform kinetic energy gradient. *J. Turbul.* **16** (5), 442–459.

TILLMARK, N. & ALFREDSSON, P. H. 1992 Experiments on transition in plane couette flow. *J. Fluid Mech.* **235**, 89–102.

VALENTE, P. C. & VASSILICOS, J. C. 2011 The decay of turbulence generated by a class of multiscale grids. *J. Fluid Mech.* **687**, 300–340.

VANDERWEL, C. & TAVOULARIS, S. 2014 Measurements of turbulent diffusion in uniformly sheared flow. *J. Fluid Mech.* **754**, 488–514.

WILSON, D. K. 1998 A new model for turbulence spectra and correlations based on Meijer's G-functions. *Technical Note* ARL-TN-104. Army Research Laboratory.

ZHU, W., VAN HOUT, R., LUZNIK, L., KANG, H. S., KATZ, J. & MENEVEAU, C. 2006 A comparison of PIV measurements of canopy turbulence performed in the field and in a wind tunnel model. *Exp. Fluids* **41** (2), 309–318.

https://doi.org/10.1017/jfm.2018.387 Published online by Cambridge University Press